Continuum modeling of micro-particle electrorotation in Couette and Poiseuille flows-The zero spin viscosity limit

Hsin-Fu Huang, Markus Zahn, Elisabeth Lemaire

Continuum Modeling of Micro-particle Electrorotation in Couette and Poiseuille Flows—the Zero Spin Viscosity Limit

Hsin-Fu Huang [a, b], Markus Zahn *[, b], Elisabeth Lemaire [c]

[a] *Department of Mechanical Engineering, Massachusetts Institute of Technology, Cambridge, MA 02139, USA*

[b] *Laboratory for Electromagnetic and Electronic Systems, Research Laboratory of Electronics, Department of Electrical Engineering and Computer Science, Massachusetts Institute of Technology, Cambridge, MA 02139, USA*

[c] *Laboratoire de Physique de la Matière Condensée, CNRS-Université de Nice-Sophia Antipolis, 06108 Nice cedex 2, France*

Abstract

A continuum mechanical model is presented to analyze the negative electrorheological responses of a particle-liquid mixture with the suspended micro-particles undergoing Quincke rotation for both Couette and Poiseuille flow geometries by combining particle electromechanics and continuum anti-symmetric/couple stress analyses in the zero spin viscosity limit. We propose a phenomenological polarization relaxation model to incorporate both the micro-particle rotation speed and macro-continuum spin velocity effects on the fluid polarization during non-equilibrium motion. Theoretical predictions of the Couette effective viscosity and Poiseuille flow rate obtained from the present continuum treatment are in good agreement with the experimental measurements reported in current literature.

Keywords: Electrohydrodynamics; Electrorotation; Quincke rotation; Negative electrorheological effect; Continuum anti-symmetric/couple stress tensor

*Corresponding author: TEL: +1-617-253-4688; FAX: +1-617-258-6774; *E-mail address*: zahn@mit.edu (Prof. M. Zahn)

1. Introduction

Electrorheological (ER) fluids are a class of fluids that consist of conducting or insulating dielectric solid micro-particles suspended within a dielectric liquid medium. Due to the electrical property (*e.g.*, conductivity and/or permittivity) mismatch between the solid and liquid phases, one can control the apparent macroscopic properties of the ER fluid such as the effective viscosity for suspensions via the application of external direct current (DC) or alternating current (AC) electric fields. Literature has therefore categorized ER effects, based on the flow or rheological responses, into either positive ER or negative ER phenomena when the fluid suspension is subjected to electric fields [1-6].

Upon the application of DC electric fields, Foulc *et al.* [4] discussed the important role of electrical conductivities of the respective solid and liquid phases in determining the inter-particle electrical force interactions in ER fluids. Boissy *et al.* [5] then further characterized and made distinctions of macroscopic positive and negative ER responses based on different relative magnitudes of the respective conductivities of the two phases. For ER fluids consisting of micro-particles with a conductivity, σ_2, larger than that, σ_1, of the carrier liquid, stable particle chains are formed in the direction of the electric field so that the macroscopic fluid resistance against externally applied shear perpendicular to the electric field is enhanced and result in an increased measured effective viscosity—the positive ER effect [1-3]. On the other hand, when the conductivity of the carrier liquid is larger than that of the micro-particles, *i.e.*, $\sigma_1 > \sigma_2$, laminated layers (perpendicular to the electric field) of packed particles resulting from electromigration are formed adjacent to one of the two electrodes leaving a portion of the ER fluid relatively clear of particles and hence leading to a reduction in the resistance against externally applied shear forces perpendicular to the electric field; a decrease in the effective viscosity is measured—the negative ER effect [5, 6].

Despite the relatively sparse reports on negative ER effects, recent experimental observations found that: (i) with a given constant shear rate or equivalently the Couette boundary driving velocity, the measured shear stress required to drive the Couette ER fluid flow is reduced (an effectively decreased viscosity) and (ii) at a given constant pressure gradient, the Poiseuille flow rate of the ER fluid can be increased both by applying a uniform DC electric field perpendicular to the direction of the flows [7-12]. The mechanism responsible for the apparent increased flow rate and decreased effective viscosity was attributed to the spontaneous electrorotation of the

dielectric micro-particles suspended within the carrier liquid, which is a mechanism different from the traditional electromigration or particle electrophoresis explanation as mentioned in previous negative ER literature [5, 6]. This spontaneous particle rotation under the action of a DC electric field is often called "Quincke rotation" for G. Quincke's systematic study done in 1896 [13-18].

The origin of Quincke rotation can be illustrated by considering a dilute collection of insulating dielectric spherical particles with permittivity ε_2 and conductivity σ_2 suspended in a slightly conducting carrier liquid having a permittivity of ε_1 and a conductivity of σ_1. The material combination is chosen so that $\tau_2 > \tau_1$ where $\tau_1 = \varepsilon_1/\sigma_1$ and $\tau_2 = \varepsilon_2/\sigma_2$ are the charge relaxation time constants of the liquid and the particles, respectively. When a uniform DC electric field is applied across the dilute suspension, charge relaxation follows the Maxwell-Wagner polarization at the solid-liquid interfaces, and each of the suspended particles attains a final equilibrium dipole moment in the opposite direction to that of the applied DC field for the condition of $\tau_2 > \tau_1$. This, however, is an unstable equilibrium, and as the applied electric field reaches a critical value [17, 18], namely,

$$E_c \equiv \left(1+\frac{\sigma_2}{2\sigma_1}\right)\sqrt{\frac{8\eta_0\sigma_1}{3\varepsilon_1\sigma_2(\tau_2-\tau_1)}}, \tag{1}$$

where η_0 is the viscosity of the carrier liquid, the liquid viscous dampening can no longer withstand any small perturbations misaligning the particle dipole moment and the applied DC field. The electrical torque resulting from the misalignment exceeds the viscous torque exerted on the micro-particle giving rise to spontaneous, self-sustained particle rotation either clockwise or counter clockwise with the rotation axis perpendicular to the planes defined by the electric field. When the particle-liquid suspension, or ER fluid, is driven by a boundary shear stress (Couette flow) or a pressure gradient (Poiseuille flow), the macroscopic flow vorticity gives the suspended micro-particles, instead of by random chance, preferable directions for rotation via viscous interactions once the external electric field (generally larger than the critical field, E_c) is applied. It is this combined effect of microscopic electrorotation and macroscopic flow vorticity that gives rise to the newly observed negative ER phenomenon as described above [7-12].

Although models are given in current literature for analyzing the new phenomenon, they are focused on the dynamics of a single particle and the utilization of a two-phase volume averaged,

effective medium description [7-12, 19]. Little has been done in developing a continuum mechanical model from a more classical field theory based starting point in predicting the dynamical behavior of fluids consisting of micro-particles undergoing spontaneous electrorotation. To the best of the authors' knowledge, the ferrofluid spin-up flow is the most representative flow phenomenon arising from internal particle rotation in current rheology research [20-27].

In a ferrofluid spin-up flow, magnetic torque is introduced into the ferrofluid, which consists of colloidally stabilized magnetic nanoparticles (typically magnetite) suspended in a non-magnetizable liquid, through the misalignment of the particle's permanent magnetization and the applied rotating magnetic field. The internal angular momentum of a continuum ferrofluid 'parcel' (containing a representative collection of liquid molecules and rotating magnetic nanoparticles) becomes significant and the continuum stress tensor becomes anti-symmetric for strong enough magnetic body torques introduced at the microscopic level. A moment-of-inertia density is defined for the ferrofluid parcel based on the mass distributions of the liquid molecules and magnetic particles in the parcel. A continuum spin velocity (column vector) is then defined by the product of the internal angular momentum density (column vector) with the inverse of the moment-of-inertia density (tensor) [28-30]. Since a ferrofluid continuum contains an enormous amount of these parcels, the spin velocity, $\overline{\omega}$, is defined as a continuous field quantity which in general, can be a function of space and time, *i.e.*, $\overline{\omega}=\overline{\omega}\left(x,y,z,t\right)$. In order to describe how microscopic particle rotation affects the continuum flow motion, a continuum angular momentum conservation equation is added and coupled with the linear momentum equation so that, in general, the externally applied magnetic body couple, angular momentum conversion between linear and spin velocity fields, and the diffusive transport of angular momentum are incorporated into the description of the flow momentum balances [22, 28-31].

A fundamental issue in the current development of ferrofluid spin-up flow is whether the diffusive angular momentum transport or couple stress has a finite contribution to the angular momentum balances of the flow. The current consensus is that the couple stress contribution is vanishingly small, *i.e.*, zero spin viscosity or diffusive transport conditions, as discussed in Rosensweig [22], Chaves *et al.* [26, 27], and Schumacher *et al.* [32]. In a most recent work by Feng *et al.* [33], scaling and numerical analyses were presented to show that in the limit of an effective continuum, the angular momentum equation is to be couple stress free and the value of

the spin viscosity should be identically zero. However, spin-up velocity profiles measured by ultrasound velocimetry reported by He [23], Elborai [24], and Chaves *et al.* [26, 27] were compared with the numerical simulations of the full spin-up flow governing equations and found that the experimental and numerical results would agree only if the spin viscosity assumes some finite value instead of being vanishingly small or identically zero.

Acknowledging the experimental and theoretical discrepancies in the value of spin viscosity and identifying the "mathematically analogous, physically parallel mechanisms" governing the respective electrorotation and ferrofluid spin-up flows as summarized in Table 1, this work is therefore aimed at developing a classical continuum mechanical model that combines particle electrorotation and anti-symmetric/couple stress theories for describing the electrorheological behavior of a particle-liquid mixture (termed ER fluid henceforward) subjected to a DC electric field strength higher than the Quincke rotation threshold in both Couette and Poiseuille flow geometries. Using a set of continuum modeling field equations similar to that utilized in ferrofluid spin-up flow analyses, we investigate the effects of a zero spin viscosity, $\eta' = 0$, *i.e.*, zero diffusive transport of angular momentum or couple stress free conditions, on the angular momentum balances in the present negative ER fluid flow of interest. In the next section, the governing equations describing the mass conservation, linear momentum conservation, angular momentum conservation, and polarization relaxation of the ER fluid flow will be given in their most general forms. The specific governing equations, analytical expressions of the spin velocity solutions, and the evaluated numerical results are then presented, compared, and discussed in Sections 3 and 4 to respectively show how the pertinent physical parameters are related to the ER responses and fluid flow for two dimensional (2D) Couette and Poiseuille flows with internal micro-particle electrorotation. A conclusion is given at the end of this article to summarize the principle findings and the motivations for future research.

2. General Formulation

In order to quantitatively model and describe the present ER flow phenomenon, several physical principles involved are considered: (i) the continuity or mass conservation, (ii) the linear momentum balance, (iii) the angular momentum balance, and (iv) the polarization relaxation of

the ER fluid flow. The governing equations are given in the following subsections to describe the above physical principles in proper mathematical forms.

2.1 The Fluid Mechanical Equations

The continuum equations describing the ER fluid motion are the mass continuity equation for incompressible flow,

$$\nabla \cdot \bar{v} = 0, \tag{2}$$

the linear momentum equation,

$$\rho \frac{D\bar{v}}{Dt} = -\nabla p + \left(\bar{P}_t \cdot \nabla\right)\bar{E} + 2\zeta \nabla \times \bar{\omega} + \beta \nabla\left(\nabla \cdot \bar{v}\right) + \eta_e \nabla^2 \bar{v}, \tag{3}$$

and the angular momentum equation,

$$I \frac{D\bar{\omega}}{Dt} = \bar{P}_t \times \bar{E} + 2\zeta\left(\nabla \times \bar{v} - 2\bar{\omega}\right) + \beta' \nabla\left(\nabla \cdot \bar{\omega}\right) + \eta' \nabla^2 \bar{\omega}, \tag{4}$$

where $\bar{v}$ is the linear flow velocity, ρ is the ER fluid density, p is the hydrodynamic pressure in the flow field, $\bar{P}_t$ is the fluid total polarization, $\bar{E}$ is the electric field, $\bar{\omega}$ is the flow spin velocity, I is the average moment of inertia per unit volume, η' is the spin viscosity, ζ is the vortex viscosity which is related to the carrier liquid viscosity, η_0, and particle solid volume fraction, ϕ, through $\zeta \sim 1.5\phi\eta_0$ for dilute suspensions with $\phi \ll 1$, $\beta = \lambda + \eta - \zeta$ is the sum of the second coefficient of viscosity, λ, the zero field ER fluid viscosity, $\eta \sim \eta_0\left(1 + 2.5\phi\right)$, and the negative of the vortex viscosity, $\eta_e = \eta + \zeta$ is the sum of the zero field ER fluid viscosity and the vortex viscosity, $\beta' = \eta' + \lambda'$ is the sum of the spin viscosity and the second coefficient of spin viscosity, λ' [19, 22, 30], and D/Dt is the material derivative given by

$$\frac{D}{Dt} = \frac{\partial}{\partial t} + \left(\bar{v} \cdot \nabla\right). \tag{5}$$

Note that Eq. (3) generally follows the form of the well known Navier-Stokes equation. However, by introducing micro-particle rotation to the fluid flow, additional terms are included in Eq. (3) to account for the Kelvin body force density, $\left(\bar{P}_t \cdot \nabla\right)\bar{E}$, and the anti-symmetric force density, $2\zeta \nabla \times \bar{\omega}$, as contributions in the linear momentum balances of the fluid flow. Moreover, Eq. (4) characterizes the ER fluid parcel spin velocity, $\bar{\omega}$, so that the torque and angular

momentum balances resulting from the electrical torque input and fluid motion can be described and related to other variables pertinent to this problem. In Eq. (4), the left hand side represents the angular momentum per unit volume of a continuum ER fluid parcel; the first term on the right hand side (RHS) represents the electrical torque density introduced to the flow field via the rotating micro-particles under the action of the external DC field; the second term on the RHS represents the angular momentum density transformation or conversion between the vorticity and the spin velocity fields; the third term on the RHS represents the gradient of the divergence of the spin velocity and is analogous to the "gradient of the divergence of the velocity" term in Eq. (3) that measures the bulk compression effects in the fluid flow; and finally, the last term on the RHS represents the diffusive transport of angular momentum within the flow field [22].

2.2 The Equilibrium Polarization and Polarization Relaxation Equations

The electric field in the ER flow field is generally described by the electro-quasi-static (EQS) Maxwell equations [16, 34], namely,

$$\nabla \times \overline{E} \approx 0, \text{ and} \tag{6}$$

$$\nabla \cdot \overline{D} = \rho_f \approx 0, \tag{7}$$

where $\overline{D}$ is the electric displacement field and ρ_f is the free space charge density. Here, we have assumed that on the macroscopic continuum level, the free space charge density is zero.

To complete the description of the electrical subsystem, we need a continuum phenomenological polarization relaxation equation that accounts for the non-equilibrium effects of both the linear and angular motions on the ER fluid polarization. Since the torque input on the micro scale is related to the induced surface charge around the surface of the micro-particles, we shall focus on how non-equilibrium motion, *i.e.*, micro-particle rotation, $\overline{\Omega}$, continuum fluid spin velocity, $\overline{\omega}$, and continuum fluid velocity, $\bar{v}$, affects the *retarding polarization*, $\overline{P}$ (the part of polarization directly related to the surface charges [7-12]), instead of the total polarization of the ER fluid, $\overline{P}_t$. Note that by definition, the spin velocity, $\overline{\omega}$, and the linear velocity, $\bar{v}$, are continuum variables which are related to respective averages of the internal angular momentum and linear momentum over collections of micro-particles and carrier liquid molecules in an ER fluid parcel. They should be distinguished from the micro-particle rotation velocity, $\overline{\Omega}$, which is the microscopic angular velocity of the suspended micro-particles within an ER fluid parcel.

We start the development of the polarization relaxation equation and its equilibrium polarization from the micro scale. The governing equation for the two region problem of the EQS fields within ($r<R$) and outside ($r>R$) a spherical solid particle suspended in a liquid medium rotating at a constant speed, $\overline{\Omega}=\Omega\overline{i}_x$, subjected to a uniform electric field, $\overline{E^\dagger}=E_z^\dagger\overline{i}_z=E_0\overline{i}_z$ ($\dagger$ denotes microscopic field quantities), as shown in Fig. 1 is the Laplace's equation in spherical coordinates,

$$\nabla^2\Phi^\dagger=\frac{1}{r^2}\frac{\partial}{\partial r}\left(r^2\frac{\partial\Phi^\dagger}{\partial r}\right)+\frac{1}{r^2\sin\theta}\frac{\partial}{\partial\theta}\left(\sin\theta\frac{\partial\Phi^\dagger}{\partial\theta}\right)+\frac{1}{r^2\sin^2\theta}\frac{\partial^2\Phi^\dagger}{\partial\phi^2}=0, \tag{8}$$

where R is the radius of the micro-particle and $\Phi^\dagger$ is the electric potential, *i.e.*, $\overline{E^\dagger}=-\nabla\Phi^\dagger$. The boundary conditions on Eq. (8) are the electric field strength far away from the micro-particle,

$$\overline{E^\dagger}\to E_0\overline{i}_z=E_0\left(\cos\theta\overline{i}_r-\sin\theta\overline{i}_\theta\right)\ \text{as}\ r\to\infty, \tag{9a}$$

the continuity of the electric potential at the solid-liquid interface,

$$\Phi^\dagger\left(r=R^-,\theta,\phi\right)=\Phi^\dagger\left(r=R^+,\theta,\phi\right), \tag{9b}$$

and charge conservation at the rotating micro-particle surface,

$$\overline{n}\cdot\left[\!\left[\overline{J_f^\dagger}\right]\!\right]+\nabla_\Sigma\cdot\overline{K_f^\dagger}=0\ \text{at}\ r=R, \tag{9c}$$

in which $\overline{n}=\overline{i}_r$ is the normal vector of the spherical surface, $\overline{J_f^\dagger}=\sigma\overline{E^\dagger}$ is the Ohmic current per unit area, $\overline{n}\cdot\left[\!\left[\overline{J_f^\dagger}\right]\!\right]=\sigma_1E_r^\dagger\left(r=R^+,\theta,\phi\right)-\sigma_2E_r^\dagger\left(r=R^-,\theta,\phi\right)$ with $E_r^\dagger$ being the r component of the electric field, $\nabla_\Sigma=\left(\overline{\overline{I}}-\overline{n}\overline{n}\right)\cdot\nabla$ is the surface divergence, and $\overline{K_f^\dagger}=\sigma_f\overline{V}$ is the surface current density with $\sigma_f=\varepsilon_1E_r^\dagger\left(r=R^+,\theta,\phi\right)-\varepsilon_2E_r^\dagger\left(r=R^-,\theta,\phi\right)$ and $\overline{V}=\Omega\overline{i}_x\times R\overline{i}_r=-\Omega R\cdot\left(\sin\phi\overline{i}_\theta+\cos\theta\cos\phi\overline{i}_\phi\right)$. Using Eqs. (8) and (9), the electric potentials and electric fields within and outside the rotating micro-particle can be solved by the method of separation of variables with the aid of associated Legendre polynomials. This problem has been solved by Cebers [35]; here, we only summarize the solutions to the electric potential and the effective dipole moment of the particle for $r>R$. The outer electric potential ($r>R$) is given in spherical coordinates as

$$\Phi^{\dagger}(r,\theta,\phi) = -rE_0\cos\theta + \frac{\overline{p_t^{\dagger}}\cdot\overline{i_r}}{4\pi\varepsilon_1 r^2} = -rE_0\cos\theta + \frac{4\pi\varepsilon_1}{4\pi\varepsilon_1 r^2}\left(a_3\cos\theta + a_6\sin\phi\sin\theta\right), \tag{10}$$

where

$$a_3 = E_0 R^3\left[\frac{\varepsilon_2-\varepsilon_1}{2\varepsilon_1+\varepsilon_2} + \frac{\left(\frac{\sigma_2-\sigma_1}{2\sigma_1+\sigma_2} - \frac{\varepsilon_2-\varepsilon_1}{2\varepsilon_1+\varepsilon_2}\right)}{1+\tau_{MW}^2\Omega^2}\right], \tag{11}$$

$$a_6 = -E_0 R^3\frac{\left(\frac{\sigma_2-\sigma_1}{2\sigma_1+\sigma_2} - \frac{\varepsilon_2-\varepsilon_1}{2\varepsilon_1+\varepsilon_2}\right)\tau_{MW}\Omega}{1+\tau_{MW}^2\Omega^2}, \tag{12}$$

$$\overline{p_t^{\dagger}} = p_x^{\dagger}\overline{i_x} + p_y^{\dagger}\overline{i_y} + p_z^{\dagger}\overline{i_z}, \tag{13}$$

$$\overline{i_r} = \sin\theta\cos\phi\overline{i_x} + \sin\theta\sin\phi\overline{i_y} + \cos\theta\overline{i_z}, \tag{14}$$

and

$$\tau_{MW} \equiv \frac{2\varepsilon_1+\varepsilon_2}{2\sigma_1+\sigma_2}, \tag{15}$$

is the Maxwell-Wagner relaxation time. With Eqs. (10)-(14), we can find the total dipole moment of the rotating particle, $\overline{p_t^{\dagger}}$, as $p_x^{\dagger}=0$, $p_y^{\dagger}=4\pi\varepsilon_1 a_6$, and $p_z^{\dagger}=4\pi\varepsilon_1 a_3$, and the *retarding part* of the dipole moment is then found as

$$\overline{p^{\dagger}} = 4\pi\varepsilon_1 a_6\overline{i_y} + 4\pi\varepsilon_1\left(a_3 - E_0R^3\frac{\varepsilon_2-\varepsilon_1}{2\varepsilon_1+\varepsilon_2}\right)\overline{i_z}. \tag{16}$$

The surface charge around the spherical particle with half of the hemisphere having positive charge and the other half having negative charge is directly related to the retarding dipole moment given by Eq. (16) [35]. By applying a torque balance between the electric torque, $\overline{p_t^{\dagger}}\times\overline{E^{\dagger}} = \overline{p^{\dagger}}\times\overline{E^{\dagger}} = 4\pi\varepsilon_1 a_6 E_0\overline{i_x}$, and the viscous torque, $-8\pi\eta_0\Omega R^3\overline{i_x}$, on the particle in steady state, we can find the critical electric field for Quincke rotation as given in Eq. (1) and the rotation velocity of the micro-particle being [18]

$$\Omega = \begin{cases} \pm \dfrac{1}{\tau_{MW}} \sqrt{\left(\dfrac{E_0}{E_c}\right)^2 - 1}, & E_0 \geq E_c \\ 0, & E_0 < E_c \end{cases}, \tag{17}$$

where the + and - signs denote counter clockwise and clockwise rotation with the coordinate system defined in Fig. 1. In Eq. (17), we have assumed that the particle rotation is only in the *x*-direction; this is because we will only be considering 2D flow geometries in the following discussions. Note however that for the most general cases, the particle rotation axis is perpendicular to the planes defined by the electric field, which has a three dimensional feature.

We next consider a dilute particle suspension with a solid volume fraction of ϕ and a particle number density of n subjected to the DC electric field. The solid volume fraction and the particle number density are related through

$$\phi = n\left(\frac{\pi d^3}{6}\right) \sim O\left(nR^3\right), \tag{18}$$

where $d = 2R$ is the diameter of the micro-particle. Assuming that the mutual electrical interactions between the suspended micro-particles can be neglected (*i.e.*, dilute suspension with $\phi \ll 1$), the macroscopic *retarding* polarization of the ER fluid at equilibrium, $\overline{P_{eq}}$, can be obtained by multiplying Eq. (16) with the particle number density, n, *i.e.*, $\overline{P_{eq}} = n\overline{p^{\dagger}} = P_{eq}^{y}\overline{i}_y + P_{eq}^{z}\overline{i}_z$, with

$$\begin{bmatrix} P_{eq}^{y} \\ P_{eq}^{z} \end{bmatrix} = 4\pi\varepsilon_1 nR^3 \begin{bmatrix} -\dfrac{\tau_{MW}\Omega\left(\dfrac{\sigma_2-\sigma_1}{2\sigma_1+\sigma_2} - \dfrac{\varepsilon_2-\varepsilon_1}{2\varepsilon_1+\varepsilon_2}\right)}{1+\tau_{MW}^2\Omega^2} \\ \dfrac{\left(\dfrac{\sigma_2-\sigma_1}{2\sigma_1+\sigma_2} - \dfrac{\varepsilon_2-\varepsilon_1}{2\varepsilon_1+\varepsilon_2}\right)}{1+\tau_{MW}^2\Omega^2} \end{bmatrix} E_0 . \tag{19}$$

Equation (19) represents the macroscopic retarding polarization of a static, motionless ER fluid, namely, $\overline{\omega} = 0$ and $\overline{v} = 0$. However, this does not mean that at macroscopic equilibrium, the micro-particles cannot rotate on the microscopic level, *i.e.*. $\overline{\Omega} \neq 0$, when the applied electric field is larger than the critical electric field given in Eq. (1), that is, $E_0 \geq E_c$. This formulation is similar to the dynamic effective medium model shown by Xiao *et al.* [36]. As for the cases of

$E_0 < E_c$, Ω is set to zero in Eq. (19) since an applied field less than the critical field will give imaginary values of Ω and the real root can only be zero as in Eq. (17). Note that by setting the micro-particle rotation speed Ω to zero, the equilibrium retarding polarization shown in Eq. (19) reduces back to the one given by Cebers [35], *i.e.*, all micro-particle rotation speed, continuum linear velocity, and continuum spin velocity equal to zero. Combining Eqs. (17) and (19) and extending the physical arguments of the phenomenological magnetization relaxation equation proposed by Shliomis [22, 37, 38] to the case of the retarding polarization, we arrive at the following retarding polarization relaxation equation,

$$\frac{D\overline{P}}{Dt} = \left(\overline{\omega} \times \overline{P}\right) - \frac{1}{\tau_{MW}}\left(\overline{P} - \overline{P_{eq}}\right), \tag{20}$$

where $\overline{P}$ is the retarding polarization.

Equations (17), (19), and (20) account for the non-equilibrium effects of the micro-particle rotation velocity, $\overline{\Omega}$, ER fluid spin velocity, $\overline{\omega}$, and ER fluid linear velocity, $\bar{v}$, on the retarding polarization. In the development of Eqs. (17), (19), and (20), we have assumed that the induced dipole moment on the micro-particles obeys the Maxwell-Wagner polarization—the induced charges are distributed on the surface of the particles at the micro scale. We have also assumed that only the retarding part of the macroscopic ER fluid polarization, *i.e.*, the polarization directly related to the interfacial charges, needs to be relaxed according to the non-equilibrium motions. Unlike the ferrofluid equilibrium magnetization, the equilibrium retarding polarization, Eq. (19), does not follow a Langevin function [22]. This is because we are considering the rotation of micro-sized dielectric insulating particles on which Brownian motion has little influence [18]. Rigorously speaking, the micro-particle rotation speed, Ω, that enters Eqs. (19) and (20) should be the speed observed in the reference frame that rotates with the ER fluid parcel. Yet, the mathematical analysis of this ER fluid flow will become much more involved and impractical in attempts to correct for the difference in reference frames, and is beyond the scope of this work. As a first approach, we employ Eq. (17) in Eqs. (19) and (20) to incorporate both microscopic (*i.e.*, $\overline{\Omega}$) and macroscopic (*i.e.*, $\overline{\omega}$ and $\bar{v}$) motions under one continuum mechanical framework.

3. Couette Flow with Internal Micro-particle Electrorotation

3.1 The Governing Equations Specific to the Couette Flow Geometry

Consider the Couette flow geometry shown in the schematic diagram of Fig. 2. The lower plate of the parallel plate system is fixed at zero velocity while the upper plate is applied with a constant velocity, U_0, in the positive *y*-direction. We assume that the flow is steady ($\partial/\partial t = 0$), incompressible, fully developed ($\partial/\partial y = 0$), and two-dimensional ($\partial/\partial x = 0$) in Cartesian coordinates. Under these assumptions, the continuity equation, Eq. (2), with $\bar{v} = u_y \bar{i}_y + u_z \bar{i}_z$ is readily reduced to $du_z/dz = 0$ and subsequently to $u_z = 0$ since the *z*-velocity component, u_z, has to satisfy the no-slip and non-penetrating (impermeable walls) boundary conditions at $z = 0$ and h with h being the height of the 2D channel. Moreover, by using the EQS Faraday's equation, Eq. (6), with $\bar{E} = E_y \bar{i}_y + E_z \bar{i}_z$ and the condition of fully developed flow, we find $dE_y/dz = 0$ such that E_y is just a constant throughout the 2D channel. Noting that the boundaries at $z = 0$ and h are perfectly conducting electrodes, and that the tangential component of the electric field is continuous across the boundaries, the constant E_y is simply zero. Therefore, the applied DC electric field is to be in the *z*-direction only. The fringing effects at the ends of the channel are to be neglected.

The governing equations are further simplified by considering a zero spin viscosity, *i.e.*, $\eta' = 0$, in the angular momentum equation, Eq. (4). Given the above assumptions combined with the continuity and zero spin viscosity conditions, Eqs. (3), (4), and (20), are then simplified into the following:

$$-\tau_{MW}\omega_x P_z - \left(P_y - P_{eq}^y\right) = 0, \tag{21a}$$

$$\tau_{MW}\omega_x P_y - \left(P_z - P_{eq}^z\right) = 0, \tag{21b}$$

$$2\zeta \frac{d\omega_x}{dz} + \eta_e \frac{d^2 u_y}{dz^2} = 0, \tag{22}$$

and

$$P_y E_z + 2\zeta\left(-\frac{du_y}{dz} - 2\omega_x\right) = 0, \tag{23}$$

where u_y is the *y*-velocity component, ω_x is the *x*-spin velocity component (note: $\bar{\omega} = \omega_x \bar{i}_x$ in

2D), E_z is the z-component of the applied DC electric field, and P_y and P_z are respectively the retarding polarization components in the y- and z- directions, *i.e.*, $\overline{P} = P_y \overline{i_y} + P_z \overline{i_z}$. Note that we have substituted the total polarization, P_{ty}, with the retarding polarization, P_y, in Eq. (23). This is because the DC electric field is applied in the z-direction only with $E_y = 0$. Thus the total polarization in the y-direction comes from the dipole moment tilt of the rotating micro-particles in the micro scale, which, on the macroscopic level, is generally the y-component of the retarding polarization. Finally, the z-linear momentum equation reduces to an equation which relates only the pressure gradient to the Kelvin body force density, and thus can be treated separately from the other equations.

Substituting Eq. (19) into Eq. (21), we can solve for the y- and z- components of the retarding polarization as

$$P_y = n \frac{\alpha_y - \tau_{MW} \omega_x \alpha_z}{1 + \tau_{MW}^2 \omega_x^2} E_0, \tag{24a}$$

$$P_z = n \frac{\alpha_z + \tau_{MW} \omega_x \alpha_y}{1 + \tau_{MW}^2 \omega_x^2} E_0, \tag{24b}$$

where

$$\begin{bmatrix} \alpha_y \\ \alpha_z \end{bmatrix} = 4\pi\varepsilon_1 R^3 \begin{bmatrix} -\dfrac{\tau_{MW}\Omega\left(\dfrac{\sigma_2 - \sigma_1}{2\sigma_1 + \sigma_2} - \dfrac{\varepsilon_2 - \varepsilon_1}{2\varepsilon_1 + \varepsilon_2}\right)}{1 + \tau_{MW}^2 \Omega^2} \\ \dfrac{\left(\dfrac{\sigma_2 - \sigma_1}{2\sigma_1 + \sigma_2} - \dfrac{\varepsilon_2 - \varepsilon_1}{2\varepsilon_1 + \varepsilon_2}\right)}{1 + \tau_{MW}^2 \Omega^2} \end{bmatrix}, \tag{25}$$

with Ω given in Eq. (17). Generally speaking, the z-component of the electric field, E_z, in Eq. (23) depends on the flow linear and spin velocities, and the EQS equations, Eqs. (6) and (7), need to be solved together with the retarding polarization, Eqs. (24) and (25), linear momentum, Eq. (22), and angular momentum, Eq. (23), equations with the suitable electrical and mechanical boundary conditions applied at $z = 0$ and h. However, the coupled set of governing equations becomes much more non-linear and less practical for engineering analysis purposes. Assuming that, due to flow motion, corrections to the z-electric field, E_z, can be related to the microscopic applied electric field and the micro-particle solid volume fraction through

$$E_z \sim E_z^{\dagger} + \phi e_1 + \phi^2 e_2 + \cdots \sim E_0 + \phi e_1 + \phi^2 e_2 + \cdots, \tag{26}$$

where e_i's are the correction terms, we substitute Eq. (24a) into Eq. (23) and approximate to the first order of magnitude of the volume fraction, ϕ, $E_z \approx E_0 + \phi e_1 + \cdots$ for dilute suspensions, *i.e.*, $\phi \ll 1$, so that the electrical field equations, Eqs. (6) and (7), can be decoupled from the mechanical field equations, Eqs. (2)-(4), or Eqs. (22) and (23). Hence the governing equations specific to the Couette flow geometry with internal particle electrorotation is obtained as Eq. (22) and

$$\frac{\alpha^* - \tau_{MW}\omega_x}{1+\tau_{MW}^2\omega_x^2} n\alpha_z E_0^2 + 2\zeta\left(-\frac{du_y}{dz} - 2\omega_x\right) = 0. \tag{27}$$

where $\alpha^* = \alpha_y / \alpha_z = -\tau_{MW}\Omega$. In Eq. (27), the first order correction, e_1, to the *z*-electric field has been neglected because e_1 has become a second order term after being substituted into Eq. (23), *i.e.*, $n\alpha_z E_0 E_z \approx n\alpha_z E_0 \left(E_0 + \phi e_1 + \cdots\right)$ with $\phi \ll 1$ and $n\alpha_z \sim nR^3 \sim nd^3 \sim O(\phi)$ as in Eq. (18). The boundary condition for the velocity field, $\bar{v} = u_y \bar{i}_y$, is the general no-slip boundary condition, *i.e.*, $\bar{v} = 0$ at $z = 0$ and $\bar{v} = U_0 \bar{i}_y$ at $z = h$. On the other hand, the angular momentum equation, Eq. (27), eventually reduces to an algebraic equation for zero spin viscosity conditions as will be discussed shortly in Section 3.2; hence, there are no additional constraints to be applied at the boundaries for the Couette spin velocity field. This "free-to-spin" condition on ω_x for $\eta' = 0$ is likely an analogous case to the Euler equation for inviscid fluid flow—the linear flow velocity is allowed to slip at the solid-fluid boundaries when the fluid viscosity goes to zero.

3.2 Solutions to the Spin Velocity and Effective Viscosity

Integrating Eq. (22) with respect to *z*, we have

$$2\zeta\omega_x + \eta_e \frac{du_y}{dz} = C_c, \tag{28}$$

where C_c is a constant. Substituting Eq. (28) into Eq. (27), we find that the spin velocity, ω_x, does not depend on the spatial coordinate, *z*, and therefore Eq. (22) reduces to the original governing equation for simple Couette flow, *i.e.*,

$$\frac{d^2 u_y}{dz^2} = 0, \tag{29}$$

and the solution to Eq. (29) is

$$u_y(z) = \frac{U_0}{h} z. \tag{30}$$

Inserting Eq. (30) into Eq. (27) and using the following non-dimensionalization scheme, namely,

$$\omega^* = \tau_{MW}\omega_x,\ \gamma^* = \tau_{MW}\frac{U_0}{h}, \text{ and } M^* = \frac{2\zeta}{n\alpha_z E_0^2 \tau_{MW}}, \tag{31}$$

the non-dimensional angular momentum equation is obtained as

$$\omega^{*3} + \frac{\gamma^*}{2}\omega^{*2} + \left(1 + \frac{1}{2M^*}\right)\omega^* + \left(\frac{\gamma^*}{2} - \frac{\alpha^*}{2M^*}\right) = 0. \tag{32}$$

Equation (32) can be solved to obtain analytical expressions by symbolic calculation packages (Mathematica, Wolfram Research, Inc.) and the three roots of Eq. (32) are expressed as functions of γ^* and M^*. Nevertheless, it should be pointed out that not all the three roots to ω^* are likely to be physically meaningful and interpretable for the flow phenomena of interest presented herein. Moreover, each of the three roots may vary from real to complex valued (or vice versa) in different parametric regimes. In order to find the most physically meaningful and interpretable solution or combination of solutions from the three possible roots to the current problem, the following considerations and conditions are applied to the flow field: (i) only real valued solutions are considered, (ii) the ER fluid is "free-to-spin" at the solid-ER fluid boundaries since the governing physics reduce from a boundary value problem to an algebraic problem in zero spin viscosity conditions, and (iii) due to micro scale viscous interactions, the micro-particle angular velocity, $\overline{\Omega}$, should rotate in the same direction as that of the macroscopic ER flow vorticity so that the micro-particle rotation is always stable [7-12].

We have shown that the spin velocity is a constant throughout the channel when $\eta' = 0$ in the Couette geometry. Hence, ω^* assumes some finite value at the solid-ER fluid boundaries, which is readily self-consistent with the "free-to-spin" condition. To satisfy condition (iii) for $E_0 \geq E_c$, we need to substitute into Eqs. (24) and (25) the micro-particle angular velocity with the minus sign in Eq. (17) which has the same negative sign (or clockwise rotation) as the macroscale Couette flow vorticity, namely, $\nabla \times \overline{v} = -\left(du_y/dz\right)\overline{i}_x = -\left(U_0/h\right)\overline{i}_x$, with the coordinate systems

defined in Figs. 1 and 2. For $E_0 < E_c$, we employ $\Omega = 0$ (see Eq. (17)) in Eqs. (24) and (25) and pick out or select the root to the spin velocity, ω^* or ω_x, that has the same negative sign as the Couette flow vorticity. For the parametric regimes of our interests, we identify the stable and real valued solution to the spin velocity as: for $E_0 \geq E_c$ (use negative Ω value in Eqs. (17), (24), and (25)),

$$\omega_{C2}^* = -\frac{\gamma^*}{6} - \varphi_{C1}\left(1+i\sqrt{3}\right)\left[6\sqrt[3]{4}M^*\left(\varphi_{C2}+\sqrt{4\varphi_{C1}^3+\varphi_{C2}^2}\right)^{1/3}\right]^{-1} + \frac{1}{12\sqrt[3]{2}M^*}\left[\left(1-i\sqrt{3}\right)\left(\varphi_{C2}+\sqrt{4\varphi_{C1}^3+\varphi_{C2}^2}\right)^{1/3}\right], \quad (33)$$

for $E_0 \leq 0.8E_c$ (use $\Omega = 0$ in Eqs. (17), (24), and (25)),

$$\omega_{C1}^* = -\frac{\gamma^*}{6} + \varphi_{C1}\left[3\sqrt[3]{4}M^*\left(\varphi_{C2}+\sqrt{4\varphi_{C1}^3+\varphi_{C2}^2}\right)^{1/3}\right]^{-1} - \frac{1}{6\sqrt[3]{2}M^*}\left(\varphi_{C2}+\sqrt{4\varphi_{C1}^3+\varphi_{C2}^2}\right)^{1/3}, \quad (34)$$

and for $0.8E_c < E_0 < E_c$ with $\Omega = 0$ in Eqs. (17), (24), and (25), ω^* is given by both ω_{C1}^* and ω_{C2}^*, *i.e.*, Eqs. (33) and (34), where

$$\varphi_{C1} = 6M^* + 12M^{*2} - M^{*2}\gamma^{*2}, \quad (35)$$

and

$$\varphi_{C2} = -18M^{*2}\gamma^* + 72M^{*3}\gamma^* + 2M^{*3}\gamma^{*3} - 108M^{*2}\alpha^*. \quad (36)$$

Note that the results shown in Eqs. (33)-(36) are obtained under the "Solve" command of Mathematica. In $0.8E_c < E_0 < E_c$, part of the real valued solution to ω^* is given by Eq. (33) and the other part is given by Eq. (34), thus, both solutions have to be used in the evaluation of the spin velocity solutions.

The effective viscosity of Couette flows with particle electrorotation, η_{eff}, is derived by recognizing the relationship between the wall shear stress, τ_s, and the average shear rate (or the velocity of the upper plate, U_0, divided by the channel height, h) when the shear stress is held constant for a given flow or experimental condition, *i.e.*,

$$\tau_s = \eta_{eff}\frac{U_0}{h} = \eta_{eff}\frac{\gamma^*}{\tau_{MW}} = \bar{i}_z \cdot \left[\!\left[\bar{\bar{T}}\right]\!\right] \cdot \bar{i}_y, \quad (37a)$$

in which denotes the shear stress differences across the solid-liquid interface, $\bar{i}_z$ is the row

vector $\begin{bmatrix}0 & 0 & 1\end{bmatrix}$, $\bar{i}_y$ is the column vector $\begin{bmatrix}0 & 1 & 0\end{bmatrix}^t$, and $\bar{\bar{T}} = \bar{\bar{T}}_s + \bar{\bar{T}}_a$ is the total stress tensor with the symmetric part being

$$\bar{\bar{T}}_s = -p\bar{\bar{I}} + \eta\left[\nabla\bar{v} + \left(\nabla\bar{v}\right)^t\right] = \begin{bmatrix} -p & 0 & 0 \\ 0 & -p & \eta\dfrac{du_y}{dz} \\ 0 & \eta\dfrac{du_y}{dz} & -p \end{bmatrix}, \tag{37b}$$

and the anti-symmetric part being

$$\bar{\bar{T}}_a = \zeta\bar{\bar{\varepsilon}}\cdot\left(\nabla\times\bar{v} - 2\bar{\omega}\right) = \begin{bmatrix} 0 & 0 & 0 \\ 0 & 0 & \zeta\left(-\dfrac{du_y}{dz} - 2\omega_x\right) \\ 0 & -\zeta\left(-\dfrac{du_y}{dz} - 2\omega_x\right) & 0 \end{bmatrix}, \tag{37c}$$

[22]. By expanding the total stress tensor into matrix form as in Eqs. (37b) and (37c) and substituting the velocity field, Eq. (30), and the spin velocity field, Eq. (33) and/or (34), into Eq. (37), the effective viscosity defined in Eq. (37a) can be obtained as

$$\eta_{eff} = \eta_e + 2\zeta\frac{\omega^*}{\gamma^*}, \tag{38a}$$

or in dimensionless terms,

$$\eta^* \equiv \frac{\eta_{eff}}{\eta} = \frac{\eta_e}{\eta} + \frac{2\zeta}{\eta}\frac{\omega_{Ci}^*}{\gamma^*}, \tag{38b}$$

where $\omega_{Ci}^* = \omega_{C1}^*$ and/or ω_{C2}^* depending on the regimes of the electric field strength where ω_{Ci}^* become real valued, and $\eta \approx \eta_0\left(1+2.5\phi\right)$ is the zero field ER fluid (particle-liquid mixture) viscosity as defined in Section 2.1. The shear stress difference in Eq. (37a) is evaluated at $z = 0$.

3.3 Results and Discussions

After obtaining the velocity and spin velocity fields as well as the effective viscosity, we now further present the numerical evaluations of the analytical expressions given in Eqs. (33), (34), and (38). The system parameters, physical constants, and material properties used in our

evaluations follow those given in Ref. [7-12] so as to facilitate a more effective comparison between the current continuum model and the two-phase effective continuum formulation found in the literature. These data are summarized in Table 2.

Shown in Fig. 3 is the Couette spin velocity, $\omega^* = \tau_{MW}\omega_x$, given by Eq. (33), *i.e.*, $\omega^* = \omega^*_{C2}$, for $E_0 \geq E_c$ and by Eq. (34), *i.e.*, $\omega^* = \omega^*_{C1}$, for $E_0 \leq 0.8E_c$ plotted with respect to the average shear rate, $\gamma^* = \tau_{MW}U_0/h$, evaluated at $E^* = E_0/E_c = 0$, 0.4, 0.8, 1.0, 2.0, and 3.0 where $E_c = 1.3\times10^6$ (V/m) is the critical electric field for the onset of particle Quincke rotation evaluated by Eq. (1). It is learned from Fig. 3 that the magnitude of the spin velocity within the flow field increases as the applied electric field strength is increased with γ^* kept constant. On the other hand, the ER fluid spin magnitude also increases as the average shear rate, γ^*, or the applied velocity of the upper boundary, U_0, increases while the electric field strength is kept constant. As the applied electric field, E_0 or E^*, is gradually reduced, the ER fluid spin velocity gradually reduces back to the zero electric field angular velocity of a continuum fluid parcel, *i.e.*, $\omega^*_0 = -\gamma^*/2$, or half of the Couette flow vorticity, which can be readily deduced from Eq. (32) by letting $M^* \to \infty$ or $E_0 \to 0$. This solution is noted by the top most, gray line with $E^* = 0$ in Fig. 3.

Notice that for a given field strength and shear rate, the spin velocity, ω^* or ω_x, is a constant throughout the channel and, thus, does not depend on the spatial *z*-coordinate as already discussed in Section 3.2 for the Couette geometry. With the spin velocity being a constant in Eq. (22), the velocity field of Couette flow with internal micro-particle electrorotation is found to be the same as that of Couette flow *without* particles—a result consistent with those given in Shliomis [39] and Rosensweig [22]. Thus, the velocity field of Couette flow with micro-particle electrorotation in the zero spin viscosity limit is simply the linear profile given by Eq. (30).

Figure 4 shows the effective viscosity, $\eta^* = \eta_{eff}/\eta$, of Couette flow with internal micro-particle electrorotation as given in Eq. (38). The effective viscosity is plotted with respect to the average shear rate, γ^*, with the electric field strength being evaluated at $E^* = 0$, 0.4, 0.8, 1.0, 2.0, and 3.0. Again, the spin velocity solution given by Eq. (33) is employed in Eq. (38) for conditions of $E^* = E_0/E_c \geq 1$, whereas Eq. (34) is employed in Eq. (38) for $E^* \leq 0.8$. It is readily

seen that the effective viscosity decreases as the applied DC electric field strength increases. However, as the magnitude of the shear rate increases, the amount of reduction in the effective viscosity decreases regardless of the applied electric field strength. Since the effective viscosity is normalized and non-dimensionalized by the zero electric field ER fluid viscosity, η, we further point out that the value of η^* should approach one as the applied electric field goes to zero, which is a result easily found by substituting $\omega_0^* = -\gamma^*/2$ into Eq. (38). The zero electric field result is indicated by the gray line in Fig. 4. It can be seen from the figure that the predicted effective viscosities η^* approach to one when the shear rate, γ^*, goes large or when the applied electric field strength is reduced.

From Fig. 4, we find that zero or negative viscosities are attainable when the applied DC electric field strength is strong enough. By using the terms "zero or negative viscosities," we do not mean that the true fluid viscosity is zero or negative, but that the effective or apparent viscosity comes out to be zero or a negative value through performing the force balance described by Eqs. (37) and (38) when the boundary shear stress, τ_s, is maintained a constant. In experimental terms, as the applied electric field strength becomes large, the "pumping" or "conveyer belt" effect of the micro-particles undergoing electrorotation on the ER fluid continuum becomes so significant that the ER fluid spin or rotation itself, instead of some externally applied force or torque, provides the shear stress required to move the upper plate of the Couette geometry. Therefore, we may observe a finite shear rate, γ^*, or plate velocity, U_0, while the readings on the rheometer or viscometer indicate a zero torque applied to the fluid. As for negative effective viscosity conditions, the electrorotation conveyer belt is so effective that the rheometer or viscometer needs to "hold back" the Couette driving plate to maintain some value of applied torque or shear rate. Further discussions can be found in Lobry and Lemaire [7] for the rheometric experimental considerations and in Rinaldi *et al.* [40] for experimental torque measurements on ferrofluids subjected to rotating magnetic fields.

The effective viscosity solutions given by the present continuum model can be compared with the theoretical and experimental results found in Lemaire *et al.* [12] by using the same carrier liquid conductivity, $\sigma_1 = 1.5\times10^{-8}$ (S/m), and other material parameters in the numerical evaluations of the present continuum model. Using their material properties and parameters, the

corresponding critical electric field for the onset of Quincke rotation is evaluated to be $E_c \approx 0.83$ (kV/mm). We find that the continuum model predicted effective viscosity, η^*, varies in a similar trend with respect to γ^* and/or E^* as compared with the theoretical predictions from the two-phase volume averaged model (single particle dynamics based) shown in Figs. 7(a) and 7(b) of Lemaire *et al.* [12]. Unlike the model based on single particle dynamics in Ref. [12] which over estimates the reduction in effective viscosity, the present continuum model under estimates the reduction in η^* at high electric field strengths, but falls closer to the experimental data shown in Figs. 7(a) and 7(b) of Ref. [12] at relatively moderate electric field strengths, *i.e.*, $E^* = E_0/E_c \approx 1.2$ and 2.4. This comparison between our continuum model predictions and the experimental data found from Lemaire *et al.* [12] is shown in Figs. 5a and 5b for micro-particle solid volume fractions of $\phi = 0.05$ and 0.1, respectively.

4. Poiseuille Flow with Internal Micro-particle Electrorotation

4.1 The Governing Equations Specific to the Poiseuille Flow Geometry

Figure 6 shows the schematic diagram of a parallel plate Poiseuille flow. Instead of an upper plate moving at a constant velocity U_0, the upper and lower plates are now both fixed at zero velocity, and a pressure gradient, $\Gamma \equiv -\partial p/\partial y$, is applied in the positive *y*-direction, *i.e.*, $\Gamma > 0$, through the channel to drive the fluid flow. Based on the similar geometries given for both Couette and Poiseuille cases, we again assume that the flow is steady, incompressible, two-dimensional, and fully developed so that the *z*-velocity component, *i.e.*, u_z in $\bar{v} = u_y \bar{i}_y + u_z \bar{i}_z$, is identically zero and that the applied pressure gradient, Γ, is a constant for a fully developed flow. The applied DC electric field is further approximated to be only in the *z*-direction, namely, $\bar{E} = E_z \bar{i}_z$, with $E_z \approx E_0$ and E_0 being a constant across the channel height, h.

For zero spin viscosity conditions, Eqs. (3), (4), and (20) then reduce to Eqs. (21), (23), and

$$\Gamma + 2\zeta \frac{d\omega_x}{dz} + \eta_e \frac{d^2 u_y}{dz^2} = 0, \tag{39}$$

where $\bar{\omega} = \omega_x \bar{i}_x$ for our 2D geometry. After substituting Eq. (19) into Eq. (21) and solving Eqs. (21a) and (21b), we again arrive at Eqs. (24) and (25). Using Eqs. (24a) and (25) in Eq. (23), we

obtain the set of governing equations for Poiseuille flow with internal micro-particle electrorotation, that is, Eqs. (39) and (27).

Since we are considering zero spin viscosities in the angular momentum equation, the spin velocity field, $\bar{\omega} = \omega_x \bar{i}_x$, again follows the "free-to-spin" condition at the boundaries while we apply the no-slip BC, $\bar{v} = 0$, at $z = 0$ and h on the velocity field, $\bar{v} = u_y(z)\,\bar{i}_y$. Yet, for a Poiseuille geometry, the spin velocity is no longer a constant throughout the flow field, *i.e.*, $\bar{\omega} = \omega_x(z)\,\bar{i}_x$, and thus a geometric condition for the spin velocity field, namely, $\bar{\omega} \to 0$, is needed as $z \to h/2$ so as to satisfy the symmetry requirements imposed by the symmetric parallel plate Poiseuille flow boundaries [23]. Also, based on the stable rotation requirement on the rotating micro-particles, we require the micro-particle rotation speed to approach zero at the mid-plane of the flow channel, *i.e.*, $\bar{\Omega} \to 0$ as $z \to h/2$, since the macroscopically imposed Poiseuille vorticity is positive (counter clockwise rotation) in the upper half of the flow channel, negative (clockwise rotation) in the lower half of the flow channel, and thus approaches zero at the mid-plane or center of the channel.

4.2 Solutions to the Spin Velocity Profile, Linear Velocity Profile, and the Volume Flow Rate

Following a similar procedure to that of the Couette geometry case, we integrate Eq. (39) to have

$$\Gamma z + 2\zeta\omega_x + \eta_e \frac{du_y}{dz} = C_p, \tag{40}$$

where C_p is a constant. Equation (40) is then substituted into Eq. (27) so that the angular momentum equation becomes

$$\frac{\alpha^* - \tau_{MW}\omega_x}{1 + \tau_{MW}^2\omega_x^2} n\alpha_z E_0^2 + 2\zeta\left(\frac{\Gamma}{\eta_e} z + \frac{2\zeta}{\eta_e}\omega_x - \frac{C_p}{\eta_e} - 2\omega_x\right) = 0. \tag{41}$$

By applying the symmetry conditions, $\bar{\omega} \to 0$ and $\bar{\Omega} \to 0$ (*i.e.*, $\omega_x \to 0$ and $\Omega \to 0$) as $z \to h/2$, to Eq. (41) and recalling that $\alpha^* = \alpha_y/\alpha_z = -\tau_{MW}\Omega$, the constant C_p is determined to be $\Gamma h/2$, and Eq. (41) is rewritten as

$$\frac{\alpha^* - \tau_{MW}\omega_x}{1+\tau_{MW}^2\omega_x^2}\frac{n\alpha_z E_0^2}{2\zeta} + \frac{\Gamma h}{\eta_e}\left(\frac{z}{h}-\frac{1}{2}\right) - \frac{2\eta}{\eta_e}\omega_x = 0, \tag{42}$$

which is an algebraic, cubic equation with the z-coordinate being a spatially varying coefficient. Using the following non-dimensionalization scheme, namely,

$$\omega^* = \tau_{MW}\omega_x,\ z^* = \frac{z}{h},\ m^* = \frac{2\zeta\eta}{n\alpha_z E_0^2 \tau_{MW}\eta_e}, \text{ and } V^* = \frac{\Gamma h \tau_{MW}}{\eta} m^*, \tag{43}$$

Eq. (42) is non-dimensionalized and the dimensionless angular momentum equation for the Poiseuille case becomes

$$\omega^{*3} - \frac{V^*}{2m^*}\left(z^* - \frac{1}{2}\right)\omega^{*2} + \left(1+\frac{1}{2m^*}\right)\omega^* - \frac{V^*}{2m^*}\left(z^* - \frac{1}{2}\right) - \frac{\alpha^*}{2m^*} = 0. \tag{44}$$

We solve Eq. (44) by standard symbolic calculation packages (Mathematica, Wolfram Research, Inc.) to express ω^* in terms of V^*, z^*, and m^*, or equivalently, to express ω_x in terms of z, Γ, and E_0. The stability, real valued, and free-to-spin conditions are then applied to select or pick out the most physically meaningful solution or combination of solutions to the spin velocity, ω^*, from the three possible roots, *e.g.*, ω_{P1}^*, ω_{P2}^*, and ω_{P3}^*, found in solving the angular momentum equation, Eq. (44). Recall from Section 3.2 that for $E_0 \geq E_c$, we require the suspended micro-particles to rotate in the direction of the macroscopic flow vorticity, which in this case, is the Poiseuille flow vorticity direction. Based on this requirement and referring to the coordinate systems shown in Figs. 1 and 6, we apply the negative valued micro-particle rotation speed Ω, *i.e.*, clockwise or pointing into the plane, in Eq. (17) to Eqs. (24) and (25) for the lower half of the channel, *i.e.*, $0 \leq z^* < 1/2$, and the positive valued Ω, *i.e.*, counter clockwise or pointing out of the plane, in Eq. (17) to Eqs. (24) and (25) for the upper half of the channel, *i.e.*, $1/2 < z^* \leq 1$. On the other hand, for $E_0 < E_c$, we set $\Omega = 0$ in Eqs. (24) and (25) and require the real valued spin velocity ω^* to be negative in $0 \leq z^* < 1/2$ and to be positive in $1/2 < z^* \leq 1$. Figure 7 shows the real valued results of the spin velocity, ω^*, plotted with respect to the spatial coordinate, z^*, with $\Gamma = 2\times10^4$ (Pa/m) at $E^* = 1.0$, 1.01, and 1.05 for both Figs. 7a and 7b and at $E^* = 0.7$, 0.8, 0.9, 0.95, and 0.99 for Fig. 7c where $E^* = E_0/E_c$ with $E_c = 1.3\times10^6$ (V/m); the dash-dash curves represent a first root, ω_{P1}^*, the dash-dot-dash curves represent a second root,

ω_{P2}^*, and the solid gray curves represent the last root, ω_{P3}^*. Although the spin velocity profiles extend across the whole channel domain, $0 \le z^* \le 1$, the solutions for $E^* > 1$ shown in Fig. 7a are only valid for $1/2 < z^* \le 1$ since we have employed in Eqs. (24) and (25) the positive valued Ω of Eq. (17) that corresponds to the positive vorticity in $1/2 < z^* \le 1$ to satisfy the stable micro-particle rotation requirement during the numerical evaluation of the figure. Similarly, the spin velocity profiles for $E^* > 1$ shown in Fig. 7b are only valid for $0 \le z^* < 1/2$ since the negative valued particle rotation speed Ω of Eq. (17) corresponding to the negative vorticity in $0 \le z^* < 1/2$ has been employed in Eqs. (24) and (25) when evaluating the solutions throughout the whole spatial domain. For spin velocity profiles shown in Fig. 7c as well as for the $E^* = 1$ solutions shown in both Figs. 7a and 7b, we find that with $\Omega = 0$ in Eqs. (24) and (25) (note: Eq. (17) goes to zero when $E^* = 1$), the spin velocity profiles become s-shaped centered at $z^* = 0.5$, and become multi-valued with respect to the spatial coordinate, z^*, near the middle of the flow channel when $\Gamma = 2 \times 10^4$ (Pa/m) and $E^* = 0.95$~1.0. This is a similar non-linear behavior found in AC or traveling wave ferrofluid spin velocity profiles under zero spin viscosity, $\eta' = 0$, conditions as discussed in Zahn and Pioch [41, 42]. However, since multi-valued spin velocity profiles will eventually lead to linear velocity profiles that are multi-valued in space, the situation is less likely to be physical for steady, viscous, and fully developed fluid flows [41, 42]. Therefore, resolution is made by requiring $\omega^* \to \omega_{P3}^* = 0$ at $z^* = 1/2$ and discarding the ω_{P1}^* and ω_{P3}^* solutions in $0 \le z^* < 1/2$ and the ω_{P2}^* and ω_{P3}^* solutions in $1/2 < z^* \le 1$, that is, use the negative valued ω^*, *i.e.*, ω_{P2}^*, in $0 \le z^* < 1/2$ and the positive ω^*, *i.e.*, ω_{P1}^*, in $1/2 < z^* \le 1$, so that the final solution is real valued, stable, symmetric, free-to-spin, and more likely physical for $\Gamma = 2 \times 10^4$ (Pa/m) and $E^* = 0.95$~1.0 conditions. Finally, for the spin velocity profiles evaluated at $\Gamma = 2 \times 10^4$ (Pa/m) and $E^* \le 0.9$ as shown in Fig. 7c, only one root, ω_{P1}^*, is found to be valid, that is, real valued and rotation direction in the vorticity direction, throughout the spatial domain, $0 \le z^* \le 1$.

By carefully examining Figs. 7a, 7b, and 7c and applying all the above reasoning and conditions, the explicit expressions of the final solution to the spin velocity of Poiseuille flow

with internal micro-particle electrorotation is obtained for $E_0 \geq E_c$ as: (i) in $0.5 < z^* \leq 1$ (substitute positive valued Ω of Eq. (17) in Eqs. (24) and (25)),

$$\omega_{P1}^* = \frac{2V^* z^* - V^*}{12m^*} + \varphi_{P1}\left[6\sqrt[3]{4}m^*\left(\varphi_{P2} + \sqrt{\varphi_{P2}^2 + 4\varphi_{P1}^3}\right)^{1/3}\right]^{-1} - \frac{1}{12\sqrt[3]{2}m^*}\left(\varphi_{P2} + \sqrt{\varphi_{P2}^2 + 4\varphi_{P1}^3}\right)^{1/3}, \quad (45)$$

(ii) at $z^* = 0.5$,

$$\omega_{P3}^* = 0, \quad (46)$$

and (iii) in $0 \leq z^* < 0.5$ (using negative valued Ω of Eq. (17) in Eqs. (24) and (25)),

$$\omega_{P2}^* = \frac{2V^* z^* - V^*}{12m^*} - \varphi_{P1}\left(1 + i\sqrt{3}\right)\left[12\sqrt[3]{4}m^*\left(\varphi_{P2} + \sqrt{\varphi_{P2}^2 + 4\varphi_{P1}^3}\right)^{1/3}\right]^{-1} + \frac{1}{24\sqrt[3]{2}m^*}\left[\left(1 - i\sqrt{3}\right)\left(\varphi_{P2} + \sqrt{\varphi_{P2}^2 + 4\varphi_{P1}^3}\right)^{1/3}\right], \quad (47)$$

where

$$\varphi_{P1} = 24m^*\left(1 + 2m^*\right) - \left(2V^* z^* - V^*\right)^2, \quad (48)$$

and

$$\varphi_{P2} = -72m^* V^* + 288m^{*2}V^* + 2V^{*3} + 144m^* V^* z^* - 576m^{*2}V^* z^* - 12V^{*3}z^* + 24V^{*3}z^{*2} - 16V^{*3}z^{*3} - 864m^{*2}\alpha^*. \quad (49)$$

As for electric field strengths below the critical electric field, *i.e.*, $E_0 < E_c$, the micro-particle rotation speed, Ω, is set to zero in Eqs. (24) and (25), and Eq. (45) is generally valid throughout $0 \leq z^* \leq 1$ for the pressure gradients of interest with $E_0 \leq 0.9E_c$. For electric field strengths of $0.95E_c \leq E_0 < E_c$, Eqs. (45)-(47) are used with $\Omega = 0$ in Eqs. (24) and (25) during the evaluation of the spin velocity profile. The analytic expressions given above are obtained under the "Solve" command using Mathematica.

Again notice that the solution or combination of solutions given to Eq. (44) need to satisfy all the above conditions and reasoning within the parametric regimes of interest since it is less likely to be physical for solutions being complex or multi-valued. The combination of solutions, Eqs. (45)-(47), presented herein is generally for the parametric range of $E^* = E_0/E_c = 1 \sim 3$ with $E_c = 1.3\times10^6$ (V/m) and $\Gamma^* = \Gamma/\Gamma_r = 0 \sim 2$ with $\Gamma_r = 2\times10^4$ (Pa/m) in $0 \leq z^* \leq 1$, whereas Eq. (45) is generally valid for $E^* \leq 0.9$ and $0 \leq \Gamma^* \leq 2$ throughout $0 \leq z^* \leq 1$. For other parametric

regimes of particular interests, the combination of solutions and the parametric range where the solutions becomes multi-valued *may be* different from the ones discussed herein. In this case, we need to start from Eq. (44) and solve for the three roots, then simultaneously apply the stability, symmetry, real valued, and "free-to-spin" conditions to the roots to finally pick out or select the suitable and most physical combination for the desired spin velocity field just like the procedure we have shown in this section. Also notice that the jump or discontinuity made in the final spin velocity profile at $z^* = 0.5$ is permitted self-consistently by the "free-to-spin" condition for the zero spin viscosity cases studied herein. This is an analogous situation to the "inviscid" parallel shear flow with the *velocity field* being $\bar{v} = U\bar{i}_y$ for $z > 0$ and $\bar{v} = -U\bar{i}_y$ for $z < 0$ as one of the possible base solutions to Kelvin-Helmholtz instability studies.

We can always rewrite Eq. (44) and express the spatial coordinate, z^*, as a function of the spin velocity, ω^*, (*i.e.*, plot z^* by varying ω^* instead of plot ω^* by varying z^*) so as to avoid encountering complex valued solutions or transition of the real valued solution from one root to another as shown in Rosensweig [22] for ferrofluid Couette flows subjected to uniform magnetic fields. However, even by this method, we will still encounter the problem of multi-valued solutions and of finding the most physically likely solution that satisfies the stable micro-particle rotation requirement for the present electrorotation flows. Moreover, as will be shortly shown in the following, since the linear velocity profile, u^*, and the 2D volume flow rate, Q, solutions depend on integrations of the spin velocity profile, ω^*, it is much more straight forward, in terms of performing the integrations with respect to z^* without obscuring the fundamental physical meanings, to express the spin velocity as a function of the spatial coordinate, *i.e.*, $\omega^* = \omega^*\left(z^*\right)$, as compared to expressing the spatial coordinate as a function of the spin velocity, $z^* = z^*\left(\omega^*\right)$. This is why we have chosen a seemly more difficult way of tackling Eq. (44) and explained in detail about the reasoning and conditions applied during the solution process.

After substituting the spin velocity solutions, ω^* or ω_x, and $C_p = \Gamma h/2$ into Eq. (40) and also noticing that for $E^* \geq 1$, ω^* is expressed by Eqs. (45) and (47) in the respective regions of $0.5 < z^* \leq 1$ and $0 \leq z^* < 0.5$, we integrate Eq. (40) with respect to the spatial coordinate, z^*, to obtain the velocity field as: (i) for $0.5 < z^* \leq 1$,

$$u_{UP}^{*}\left(z^{*}\right)=\frac{\eta}{\eta_e}\left[z^{*}\left(1-z^{*}\right)+\frac{4\zeta}{\Gamma h\tau_{MW}}\int_{z^{*}}^{1}\omega_{P1}^{*}\left(z^{*}\right)dz^{*}\right], \tag{50a}$$

and (ii) for $0\le z^{*}<0.5$,

$$u_{DN}^{*}\left(z^{*}\right)=\frac{\eta}{\eta_e}\left[z^{*}\left(1-z^{*}\right)-\frac{4\zeta}{\Gamma h\tau_{MW}}\int_{0}^{z^{*}}\omega_{P2}^{*}\left(z^{*}\right)dz^{*}\right], \tag{50b}$$

where the velocity field, Eq. (50), is made dimensionless by dividing with $\Gamma h^2/2\eta$ (*note*: use η not η_e), *i.e.*, $u^{*}\left(z^{*}\right)=2\eta u_y\left(z^{*}\right)\big/\Gamma h^2$, ω_{P1}^{*} and ω_{P2}^{*} are respectively defined in Eqs. (45) and (47), and z^{*} is a dummy index in both equations. For $E^{*}\le 0.9$, use ω_{P1}^{*}, *i.e.*, Eq. (45), in place of ω_{P2}^{*}, *i.e.*, Eq. (47), in Eq. (50b), that is, use Eq. (45) for the spin velocities throughout $0\le z^{*}\le 1$ in the integration of Eq. (50). From general mathematical point of views, the velocity field of the flow, u_y, needs to be continuous and smooth (continuous in du_y/dz) throughout the channel because of finite ER fluid viscosities, η. However, since we have manually (with physical reasoning) made the spin velocity, ω_x, discontinuous at the middle of the channel, the smoothness of the velocity distribution near $z^{*}=0.5$ may not exactly be preserved under the framework of zero spin viscosity limits—a cusp may arise at $z^{*}=0.5$ in the velocity profile given by Eq. (50) for certain parametric regimes of interest. This issue will be further discussed in Section 4.3.

We next calculate the two dimensional volumetric flow rate, Q, by integrating the velocity fields, *i.e.*,

$$Q=\int_0^h u_y\left(z\right)dz=\frac{\Gamma h^3}{2\eta}\left[\int_0^{0.5}u_{DN}^{*}\left(z^{*}\right)dz^{*}+\int_{0.5}^{1}u_{UP}^{*}\left(z^{*}\right)dz^{*}\right], \tag{51}$$

with Eq. (50a) used for $0.5<z^{*}\le 1$ and Eq. (50b) used for $0\le z^{*}<0.5$. In terms of the spin velocities, Eq. (51) is rewritten as, for $E^{*}\ge 1$,

$$Q=\left(\frac{\Gamma h^3}{12\eta}\right)\left(\frac{\eta}{\eta_e}\right)\left\{1+\frac{24\zeta}{\Gamma h\tau_{MW}}\left[\int_{0.5}^{1}\int_{z^{*}}^{1}\omega_{P1}^{*}\left(z^{*}\right)dz^{*}dz^{*}-\int_0^{0.5}\int_0^{z^{*}}\omega_{P2}^{*}\left(z^{*}\right)dz^{*}dz^{*}\right]\right\}, \tag{52}$$

where z^{*} is the dummy index and Eqs. (45) and (47) are used in the integration ranges of $0.5<z^{*}\le 1$ and $0\le z^{*}<0.5$, respectively. Again, for $E^{*}\le 0.9$, use ω_{P1}^{*}, *i.e.*, Eq. (45),

throughout $0 \le z^* \le 1$ in the integration of Eq. (51) or (52). It is now obvious why we use η, zero electric field ER fluid viscosity, instead of $\eta_e = \eta + \zeta$ in non-dimensionalizing the velocity field of Eq. (50). The intention is to utilize the ordinary Poiseuille flow solution (no electric field applied to the ER fluid) as a reference datum so that the variation and deviation in the electrorotation modified Poiseuille velocities and flow rates from those of the zero electric field solutions, *i.e.*, $u_0^*(z^*) = (2\eta/\Gamma h^2) u_y(z^*) = z^*(1-z^*)$ and $Q_0 = \Gamma h^3/12\eta$, can be respectively compared.

Results of the spin velocity profile, (linear) velocity profile, and the volume flow rate will be respectively presented in the following subsection. The system parameters, physical constants, and material properties used in the numeric evaluations can be found in Table 2 unless otherwise specified.

4.3 Results and Discussions

Before presenting the spin velocity profiles, we first normalize the Poiseuille spin velocity, Eqs. (45)-(47) by $\Gamma h \tau_{MW}/2\eta$, namely, $\omega^* = \omega_{P1}^* = 2\eta\omega_{P1}^*/\Gamma h \tau_{MW}$ for $0.5 < z^* \le 1$, $\omega^* = \omega_{P2}^* = 2\eta\omega_{P2}^*/\Gamma h \tau_{MW}$ for $0 \le z^* < 0.5$, and $\omega^* = \omega_{P3}^* = 2\eta\omega_{P3}^*/\Gamma h \tau_{MW} = 0$ for $z^* = 0.5$. By employing this normalization, we find that the zero electric field solution, $\omega_0^* = \Gamma h \tau_{MW}(z^* - 0.5)/2\eta$, becomes independent of the applied pressure gradient and only depends on the spatial position in the channel, *i.e.*, $\omega_0^* = (z^* - 0.5)$. The zero electric field solution then becomes a reference datum invariant of both the applied electric field strength and the driving pressure gradient and facilitates a more physically meaningful comparison among the solutions.

Illustrated in Fig. 8 are the spatial variations of the electrorotation assisted Poiseuille spin velocity profiles given by Eqs. (45)-(47) normalized by $\Gamma h \tau_{MW}/2\eta$ plotted with respect to distinct strengths of the applied electric field, $E^* = E_0/E_c$. With the pressure gradient kept constant, *i.e.*, $\Gamma^* = \Gamma/\Gamma_r = 1$ where $\Gamma_r = 2\times10^4$ (Pa/m), the normalized spin velocity ω^* is evaluated at $E^* = 0$, 0.4, 0.8, 1.0, 2.0, and 3.0 with $E_c = 1.3\times10^6$ (V/m). The solid gray curve

shown in Fig. 8 represents the zero electric field solution, $\omega_0^* = \left(z^* - 0.5\right)$, or half of the Poiseuille vorticity when there is no electric field and internal micro-particle electrorotation effects. From the figure, the positive and negative valued spin velocities found in the respective regions of $0.5 < z^* \le 1$ and $0 \le z^* < 0.5$ (with $\omega^* = \omega_{P3}^* = 0$ at $z^* = 0.5$) show that we have chosen, based on the macroscopic Poiseuille vorticity directions, the combination of solutions that satisfies the symmetry, real valued, and stable particle rotation conditions. The apparent jump or discontinuity in the spin velocity profile at $z^* = 0.5$ is self-consistently permitted by the "free-to-spin" condition under the framework of the zero spin viscosity limit as already mentioned in the previous sections.

As can be seen in Fig. 8, the magnitude of the normalized spin velocity of Poiseuille flow with internal particle electrorotation increases as the applied DC electric field strength is increased. If, on the contrary, we reduce the applied electric field strength from $E^* = 1.0$, 0.8 to 0.4, we find that the spin velocity gradually approaches the zero electric field solution noted by the gray curve in Fig. 8. Moreover, the strength of the jump or discontinuity at $z^* = 0.5$ in the normalized spin velocity field reduces and eventually smoothes out (see the smooth and continuous curves for $E^* = 0.4$ and 0.8) as the applied electric field is decreased. Note that in this figure, the solutions to $E^* = 0.4$ and 0.8 are fully represented by $\omega^* = \omega_{P1}^*$, *i.e.*, Eq. (45), throughout the spatial domain, $0 \le z^* \le 1$, at $\Gamma^* = 1$. However, the spin velocity solutions to $E^* = 1.0$, 2.0, and 3.0 are represented by $\omega^* = \omega_{P1}^*$ (Eq. (45)) for $0.5 < z^* \le 1$, $\omega^* = \omega_{P2}^*$ (Eq. (47)) for $0 \le z^* < 0.5$, and zero (Eq. (46)) for $z^* = 0.5$ at $\Gamma^* = 1$. The transition among the different roots verifies the cubic nature of the governing equation, Eq. (44).

After the spin velocity field is found, the (linear) velocity field is easily obtained by integrating Eq. (50). The results of the velocity field, u^* (or u_y), are plotted with respect to the spatial coordinate z^* in Fig. 9 for $\Gamma^* = 1$ with $E^* = 0$, 0.4, 0.8, 1.0, 2.0, and 3.0. The gray solid curve represents the zero electric field solution, $u_0^* = z^*\left(1 - z^*\right)$, *i.e.*, the velocity field of ordinary Poiseuille flow without internal micro-particle electrorotation. Recall that the velocity field was already normalized by $\Gamma h^2/2\eta$ in the non-dimensional definition of Eq. (50); hence, there is no more need to define a normalized velocity field as in the case of the spin velocity.

Based upon the above convention, we find in Fig. 9 that with $\Gamma^* = 1$ kept constant, the flow velocity is considerably enhanced and the cusp in the velocity profile at $z^* = 0.5$ is sharpened as the strength of the applied DC electric field is increased. If we reduce the strength of the electric field while the pressure gradient is maintained constant, the cusp at $z^* = 0.5$ becomes blunt and the electrorotation enhanced velocity profile gradually reduces and converges back to the $E^* = 0$ solution, *i.e.*, the parabolic Poiseuille flow velocity field without internal particle electrorotation as noted by the solid gray curve in the figure. The $E^* = 0.4$ and 0.8 velocity fields shown are evaluated by substituting Eq. (45), *i.e.*, ω_{P1}^*, into the integrals of both Eqs. (50a) and (50b) with $\Omega = 0$ in Eqs. (24) and (25) since in this parametric regime, ω_{P1}^* assumes a real value and is valid throughout the spatial domain of $0 \le z^* \le 1$. As for $E^* = 1.0$, 2.0, and 3.0, Eq. (45) is employed in the integral of Eq. (50a) whereas Eq. (47) is used in Eq. (50b). The cusped velocity profiles shown in Fig. 9 are consistent with those obtained from combined single particle dynamics and two-phase effective medium modeling [9] and are interestingly similar to the velocity profiles of a power law fluid in circular pipe Poiseuille flow geometries for large power indices [43] though, of course, the electrorotation and power law fluid flows work respectively on different principles.

Finally, using the physical parameters and material properties given in Table 2, the two dimensional volume flow rate of Poiseuille flow with internal micro-particle electrorotation, Q (m^2/s), is plotted with respect to the driving pressure gradient, $\Gamma^* = \Gamma/\Gamma_r$ with $\Gamma_r = 2\times10^4$ (Pa/m), at distinct values of the applied DC electric field strength, $E^* = E_0/E_c$ with $E_c = 1.3\times10^6$ (V/m). The results are shown in Fig. 10 for $E^* = 0$, 0.4, 0.8, 1.0, 2.0, and 3.0 with the solid gray curve noted by $E^* = 0$ corresponding to the two dimensional volume flow rate of Poiseuille flow without internal micro-particle electrorotation, *i.e.*, $Q_0 = \Gamma h^3/12\eta$.

From Fig. 10, we find that the volume flow rate increases as the applied DC electric field strength is increased while the driving pressure gradient is kept constant. On the other hand, the electrorotation enhanced volume flow rate gradually reduces back to the zero electric field solution, $Q_0 = \Gamma h^3/12\eta$, as the applied electric field is reduced. These results are consistent with our previous examination of the velocity fields shown in Fig. 9 and agree with the experimental

observations reported in Ref. [10]. Note that the flow rate solutions evaluated at $E^* =$ 1.0, 2.0, and 3.0 suggest non-zero volume flow rates at zero driving pressure gradients when the flow is subjected to an applied electric field strength greater than or equal to the critical electric field for the onset of Quincke rotation. This result is particularly due to the fact that we have used the combination of solutions to the spin velocity, Eqs. (45)-(47), that satisfies the symmetry, real valued, stable micro-particle rotation, and free-to-spin conditions in the modeling and evaluation of the volume flow rate, Q, under zero spin viscosity conditions, *i.e.*, $\eta' = 0$. Nonetheless, we need to point out that unless there is some initial flow ($\Gamma^* \neq 0$) applied to give the suspended micro-particles a favorable direction for electrorotation, the direction for Quincke rotation is merely a matter of chance with the particle rotation axis either pointing into or out of the planes defined by the electric field under zero flow or equivalently zero driving pressure gradient conditions. Up to this point, no experimental evidence has observed a negative ER effect with zero initial flow when an electric field strength, $E_0 \geq E_c$, is applied [7]—both initial vorticity and micro-particle Quincke rotation are needed for the present negative ER effect. The finite jump of volume flow rate at zero driving pressure gradients diminishes and eventually becomes zero, *i.e.*, zero flow rate at zero pressure gradient, as we reduce the applied electric field strength from $E^* = 1.0$, 0.8, to 0.4 as can be found in the figure. Again, for the $E^* \leq 0.9$ solutions, *i.e.*, $E^* = 0.4$ and 0.8, shown in Fig. 10, we have used ω_{P1}^*, Eq. (45), throughout the spatial domain, $0 \leq z^* \leq 1$.

Summing up the findings from examining Figs. 8-10, it is found that, in general, the magnitude of the normalized spin velocity, the normalized flow velocity, and the 2D volume flow rate is increased as the applied electric field, E^*, is increased with the driving pressure gradient, Γ^*, kept constant. Moreover, increasing the applied electric field gives rise to a more severe jump or discontinuity at $z^* = 0.5$ in the normalized spin velocity profile, sharpens the cusp structure at $z^* = 0.5$ in the (normalized) velocity profile, and results in a finite value of volume flow rate at zero pressure gradients. Contrarily, reducing the strength of the electric field smoothes out the cusp in the velocity profile and reduces the severity of the discontinuity at $z^* = 0.5$ in the spin velocity field while the pressure gradient is kept constant. The (normalized) velocity and spin velocity profiles as well as the 2D volume flow rate gradually reduce back to the zero electric field solutions as the applied electric field strength is reduced.

Lastly, as shown in Fig. 11, the theoretical predictions of the 2D Poiseuille volume flow rate from the present continuum mechanical model are compared with the experimental data found from Figs. 5 and 6 of Lemaire *et al.* [10] by using the same material and physical parameters, *e.g.*, channel height of $h = 750$ (μm) and electric field strengths of $E_0 = 2.7$ and 3.3 (kV/mm), employed therein for micro-particle solid volume fractions of $\phi = 0.05$ (Fig. 11a) and 0.1 (Fig. 11b). The corresponding critical electric field for the onset of micro-particle Quincke rotation is evaluated as $E_c = 1.3\times10^6$ (V/m) by substituting the material properties given in Ref. [10] into Eq. (1). It can be found from Fig. 11 that the theoretical Poiseuille volume flow rate results obtained from the present continuum analysis are in good agreement with the experimental data found from Figs. 5 and 6 of Ref. [10] despite the slight over estimation in the volume flow rate as compared to the experimental data from Ref. [10]. The theoretical predictions from both the present continuum model and the previous single particle dynamics based model give similar variations of the 2D volume flow rate with respect to the applied electric field strength and pressure gradient—the volume flow rate increases as the applied electric field increases.

As a general conclusion of the results presented in this article, we find that, in the zero spin viscosity limit, the full continuum governing equations (from anti-symmetric/couple stress theories) employed in this article reduce to a "particulate limit" and predict similar trends of variations of the effective viscosities for Couette flow and of the two dimensional volume flow rates for Poiseuille flow as compared to the theoretical predictions from the two-phase volume averaged effective medium model (single particle dynamics based) found in the literature [7-12, 19] for describing the internal micro-particle electrorotation modified flow phenomena.

5. Concluding Remarks

Two dimensional Couette and Poiseuille flows with internal, spontaneous micro-particle electrorotation, or Quincke rotation, are modeled and analyzed through a fully continuum mechanical formulation in this article. By combining the theories of particle electromechanics and continuum anti-symmetric/couple stresses, general governing equations are given to describe the physical aspects of polarization relaxation, mass conservation, momentum conservation, and angular momentum conservation involved in this novel negative electrorheological phenomena. With the assumptions of steady, incompressible, fully developed, and two dimensional flows, the

general governing equations are respectively reduced to two algebraic, cubic equations of the ER fluid spin velocity, ω^*, for the Couette and Poiseuille flow geometries in the limit of a zero spin viscosity in the angular momentum equation. Stability, symmetry, and "free-to-spin" conditions are then applied to the cubic spin velocity equations to pick out or select the real valued solution or combination of solutions consistent with the physical assumptions and phenomena of interest. Expressions for the effective viscosity, η^*, of Couette flow as well as the linear velocity field, u^*, and the 2D volume flow rate, Q, of Poiseuille flow can be further derived in terms of the applied electric field, E^*, shear rate, γ^*, driving pressure gradient, Γ^*, or spatial coordinate, z^*, by respectively substituting the most physically suitable and meaningful solution or combination of solutions to the spin velocity, ω^*, into the linear momentum equation with the no-slip boundary conditions on the velocity field applied at the spatial boundaries. Modeling results are summarized in the following:

(i) With internal particle electrorotation, the spin velocity, ω^*, increases as either the applied electric field strength, E^*, or the shear rate, γ^*, is increased for Couette flow. Contrarily, the spin velocity reduces back to the zero electric field solution ($E^* = 0$, no particle electrorotation), *i.e.*, $\omega_0^* = -\gamma^*/2$, or half of the Couette flow vorticity, as the applied electric field strength is decreased. In the limit of zero spin viscosity, the linear Couette velocity profile, $u_y(z) = U_0 z/h$, remains invariant regardless of the applied electric field strength.

(ii) The effective viscosity, η^*, is found to decrease as the applied DC electric field strength increases for Couette flow with internal particle electrorotation. However, as the driving shear rate becomes large, the amount of reduction in the effective viscosity is reduced regardless of the applied electric field strength. For a decreasing electric field strength, the effective viscosity goes back to the zero electric field solution, $\eta^* = 1$, *i.e.*, the zero field viscosity of the ER fluid (particle-liquid mixture), η.

(iii) With a constant driving pressure gradient, Γ^*, the magnitude of the normalized Poiseuille spin velocity, ω^*, as well as the jump or discontinuity in the spin velocity profile increases as the applied electric field, E^*, increases whereas the spin velocity reduces back to the zero

field solution, $\omega_0^* = \left(z^* - 0.5\right)$, and the discontinuity in the spin velocity profile diminishes as E^* is reduced.

(iv) With a constant driving pressure gradient, Γ^*, the magnitude of the dimensionless (normalized) Poiseuille linear velocity, u^*, as well as the sharpness of the cusp in the velocity profile increases as the applied electric field, E^*, increases. On the contrary, the velocity profile reduces back to the zero field solution, $u_0^* = z^*\left(1 - z^*\right)$, and the cusp in the velocity profile becomes blunt as E^* is reduced.

(v) The two dimensional Poiseuille volume flow rate, Q, increases as the applied DC electric field strength increases whereas the electrorotation enhanced flow rate solution reduces back to the zero electric field solution, $Q_0 = \Gamma h^3/12\eta$, as the applied electric field is decreased. At zero driving pressure gradients, the electrorotation enhanced volume flow rate assumes some finite value because of the fact that we have employed the spin velocity solution that satisfies the symmetry, real valued, stable micro-particle rotation, and free-to-spin conditions in the evaluation of Q under zero spin viscosity conditions.

(vi) Comparing the results of the Couette effective viscosity and the Poiseuille volume flow rate obtained herein with those found in current literature, we find that both the present continuum and the previous two-phase volume averaged (single particle dynamics based) models qualitatively predict the same trends of variation for the effective viscosity with respect to the electric field strength and average shear rate, and for the volume flow rate with respect to the field strength and driving pressure gradient. The similarities found between the two modeling approaches suggest that the fully continuum mechanical modeling field equations presented in this article reduces to a "particulate limit" when the spin viscosity in the continuum angular momentum equation equals to zero, *i.e.*, couple stress free conditions. Note however that the theoretical predictions of the Couette effective viscosity and Poiseuille volume flow rate obtained from the present continuum mechanical treatment are in good agreement with the experimental measurements as reported in current literature.

Future work includes a more advanced modeling of the polarization relaxation processes in the electrorheological fluid flow, the investigation of finite spin viscosity effects on the angular

momentum balances within the flow field, and the search of possible practical applications for such novel negative electrorheological phenomenon.

Acknowledgements

H.-F. Huang is financially supported by the National Science Council (Taipei, Taiwan) through the Taiwan Merit Scholarships under grant no. TMS-094-2-A-029. This work was supported in part by the United States-Israel Binational Science Foundation (BSF) through grant no. 2004081. The authors would like to thank Prof. Mark I. Shliomis of the Department of Mechanical Engineering at the Ben-Gurion University of the Negev in Israel for fruitful and insightful discussions.

References

[1] W.M. Winslow, Induced fibration of suspensions, J. Appl. Phys. 20 (1949) 1137-1140.

[2] T.C. Halsey, Electrorheological fluids, Science 258 (1992) 761-766.

[3] D.J. Klingenberg, C.F. Zukoski IV, Studies of the steady-shear behavior of electro-rheological suspensions, Langmuir 6 (1990) 15-24.

[4] J.N. Foulc, P. Atten, N. Felici, Macroscopic model of interaction between particles in an electrorheological fluid, J. Electrost. 33 (1994) 103-112.

[5] C. Boissy, P. Atten, J.N. Foulc, On a negative electrorheological effect, J. Electrost. 35 (1995) 13-20.

[6] C.W. Wu, H. Conrad, Negative electrorheological effect and electrical properties of a Teflon/silicone oil suspension, J. Rheol. 41 (1997) 267-281.

[7] L. Lobry, E. Lemaire, Viscosity decrease induced by a DC electric field in a suspension, J. Electrost. 47 (1999) 61-69.

[8] A. Cebers, E. Lemaire, L. Lobry, Internal rotations in dielectric suspensions, Magnetohydrodyn. 36 (2000) 347-364.

[9] A. Cebers, E. Lemaire, L. Lobry, Flow modification induced by Quincke rotation in a capillary, Int. J. Mod. Phys. B 16 (2002) 2063-2069.

[10] E. Lemaire, L. Lobry, N. Pannacci, Flow rate increased by electrorotation in a capillary, J. Electrost. 64 (2006) 586-590.

[11] N. Pannacci, E. Lemaire, L. Lobry, Rheology and structure of a suspension of particles subjected to Quincke rotation, Rheol. Acta 46 (2007) 899-904.

[12] E. Lemaire, L. Lobry, N. Pannacci, F. Peters, Viscosity of an electro-rheological suspension with internal rotations, J. Rheol. 52 (2008) 769-783.

[13] G. Quincke, Ueber rotationen im constanten electrischen felde, Ann. Phys. Chem. 59 (1896) 417-486.

[14] J.R. Melcher, G.I. Taylor, Electrohydrodynamics: a review of the role of interfacial shear stresses, Annu. Rev. Fluid Mech. 1 (1969) 111-146.

[15] J.R. Melcher, Electric fields and moving media, IEEE Trans. Educ. E-17 (1974) 100-110.

[16] J.R. Melcher, Continuum Electromechanics, The MIT Press, Cambridge, MA, 1981.

[17] T.B. Jones, Quincke rotation of spheres, IEEE Trans. Ind. Appl. IA-20 (1984) 845-849.

[18] T.B. Jones, Electromechanics of Particles, Cambridge University Press, New York, NY, 1995.

[19] H. Brenner, Rheology of two-phase systems, Annu. Rev. Fluid Mech. 2 (1970) 137-176.

[20] R. Moskowitz, R.E. Rosensweig, Nonmechanical torque-driven flow of a ferromagnetic fluid by an electromagnetic field, Appl. Phys. Lett. 11 (1967) 301-303.

[21] R.E. Rosensweig, J. Popplewell, R.J. Johnston, Magnetic fluid motion in rotating field, J. Magn. Magn. Mater. 85 (1990) 171-180.

[22] R.E. Rosensweig, Ferrohydrodynamics, reprint ed., Dover Publications, Mineola, NY, 1997.

[23] X. He, Ferrohydrodynamic flows in uniform and non-uniform rotating magnetic fields, Ph.D. Dissertation, Department of Electrical Engineering and Computer Science, Massachusetts Institute of Technology, Cambridge, MA, 2006.

[24] S.M. Elborai, Ferrofluid surface and volume flows in uniform rotating magnetic fields, Ph.D. Dissertation, Department of Electrical Engineering and Computer Science, Massachusetts Institute of Technology, Cambridge, MA, 2006.

[25] A. Chaves, C. Rinaldi, S. Elborai, X. He, M. Zahn, Bulk flow in ferrofluids in a uniform rotating magnetic field, Phys. Rev. Lett. 96 (2006) 194501.

[26] A. Chaves, F. Gutman, C. Rinaldi, Torque and bulk flow of ferrofluid in an annular gap subjected to a rotating magnetic field, Trans. ASME-J. Fluid. Eng. 129 (2007) 412-422.

[27] A. Chaves, M. Zahn, C. Rinaldi, Spin-up flow of ferrofluids: asymptotic theory and experimental measurements, Phys. Fluid. 20 (2008) 053102.

[28] J.S. Dahler, L.E. Scriven, Angular momentum of continua, Nat. 192 (1961) 36-37.

[29] J.S. Dahler, L.E. Scriven, Theory of structured continua. I. General consideration of angular momentum and polarization, Proc. Roy. Soc. A 275 (1963) 504-527.

[30] D.W. Condiff, J.S. Dahler, Fluid mechanical aspects of anti-symmetric stress, Phys. Fluid. 7 (1964) 842-854.

[31] A.C. Eringen, Theory of micropolar fluids, J. Math. Mech. 16 (1966) 1-16.

[32] K.R. Schumacher, I. Sellien, G.S. Knoke, T. Cader, B.A. Finlayson, Experiment and simulation of laminar and turbulent ferrofluid pipe flow in an oscillating magnetic field, Phys. Rev. E 67 (2003) 026308.

[33] S. Feng, A.L. Graham, J.R. Abbott, H. Brenner, Anti-symmetric stresses in suspensions: vortex viscosity and energy dissipation, J. Fluid Mech. 563 (2006) 97-122.

[34] H.A. Haus, J.R. Melcher, Electromagnetic Fields and Energy, Prentice-Hall, Englewood Cliffs, NJ, 1989.

[35] A. O. Cebers, Internal rotation in the hydrodynamics of weakly conducting dielectric suspensions, Mekhanika Zhidkosti i Gaza 2 (1980) 86-93. (see also Fluid Dyn. 15 (1980) 245-251)

[36] J.J. Xiao, J.P. Huang, K.W. Yu, Dynamic polarizability of rotating particles in electrorheological fluids, J. Phys. Chem. B 112 (2008) 6767-6771.

[37] M.I. Shliomis, Certain gyromagnetic effect in a liquid paramagnet, Sov. Phys. JEPT 39 (1974) 701-704.

[38] M.I. Shliomis, Nonlinear effects in suspension of ferromagnetic particles under action of a rotating magnetic field, Sov. Phys. Dokl. 19 (1975) 686-687.

[39] M.I. Shliomis, Effective viscosity of magnetic suspensions, Sov. Phys. JETP 34 (1972) 1291-1294.

[40] C. Rinaldi, F. Gutman, X. He, A.D. Rosenthal, M. Zahn, Torque measurements on ferrofluid cylinders in rotating magnetic fields, J. Magn. Magn. Mater. 289 (2005) 307-310.

[41] M. Zahn, L.L. Pioch, Magnetizable fluid behavior with effective positive, zero, or negative dynamic viscosity, Indian J. Eng. Mater. Sci. 5 (1998) 400-410.

[42] M. Zahn, L.L. Pioch, Ferrofluid flows in AC and traveling wave magnetic fields with effective positive, zero or negative dynamic viscosity, J. Magn. Magn. Mater. 201 (1999) 144-148.

[43] R.P. Chhabra, J.F. Richardson, Non-newtonian Flow in the Process Industries: Fundamentals and Engineering Applications, Butterworth-Heinemann, Boston, MA, 1999.

Table Captions

Table 1. Summary of physical analogy between the electrorotation and ferrofluid spin-up flows.

Table 2. System parameters, physical constants, and material properties used in the numerical evaluations [7-12].

Figure Captions

Figure 1. The schematic diagram for the problem of solving the EQS fields within and outside a spherical particle of radius R (with conductivity of σ_2 and permittivity of ε_2) suspended in a liquid medium (with σ_1, ε_1) rotating at constant angular velocity $\overline{\Omega}=\Omega\overline{i}_x$ subjected to a uniform DC electric field, $\overline{E^{\dagger}}=E_0\overline{i}_z$.

Figure 2. The schematic diagram illustrating the geometry, dimensions, and physical parameters for Couette flow with internal micro-particle electrorotation.

Figure 3. The dimensionless Couette spin velocity, ω^*, plotted with respect to the average shear rate, γ^*, evaluated at $E^*=0$, 0.4, 0.8, 1.0, 2.0, and 3.0. For $E^*\geq 1.0$, the spin velocity is given by Eq. (33), *i.e.*, $\omega^*=\omega^*_{C2}$ (negative valued Ω from Eq. (17) used in Eqs. (24) and (25)), whereas for the cases of $E^*\leq 0.8$, ω^* is given by Eq. (34), $\omega^*=\omega^*_{C1}$, with the micro-particle rotation speed, Ω, set to zero in Eqs. (24) and (25). The gray line denotes the zero electric field spin velocity, namely, half of the fluid vorticity, $\omega^*_0=-\gamma^*/2$.

Figure 4. The effective viscosity, η^*, found for Couette flow plotted with respect to the average shear rate, γ^*, evaluated at $E^*=0$, 0.4, 0.8, 1.0, 2.0, and 3.0. For $E^*\geq 1.0$, the spin velocity given by Eq. (33), *i.e.*, $\omega^*=\omega^*_{C2}$, is used in the evaluation of Eq. (38), whereas for $E^*\leq 0.8$, $\omega^*=\omega^*_{C1}$ given by Eq. (34) is employed in Eq. (38). The gray line denotes the zero electric field value of the effective viscosity, *i.e.*, $\eta^*=\eta_{eff}/\eta=1$, with the value of η given in Table 2.

Figure 5. The present continuum modeling results of effective viscosity, η^*, versus average shear rate, γ^*, are compared with the experimental data found from Lemaire *et al.* [12] at electric field strengths of $E_0=1$ (diamond), 2 (triangle), and 3 (box) (kV/mm) for micro-

particle solid volume fractions of $\phi = 0.05$ (Fig. 5a) and 0.1 (Fig. 5b). Using the material properties from Ref. [12], the corresponding critical electric field for Quincke rotation is evaluated to be $E_c \approx 0.83$ (kV/mm).

Figure 6. The schematic diagram illustrating the geometry, dimensions, and physical parameters for Poiseuille flow with internal micro-particle electrorotation.

Figure 7. The three roots, ω_{P1}^*, ω_{P2}^*, and ω_{P3}^*, of the dimensionless Poiseuille spin velocity, ω^*, to the angular momentum equation, Eq. (44). The spin velocity profiles are plotted with respect to the spatial coordinate, z^*, at $\Gamma = 2\times10^4$ (Pa/m) and $E^* = E_0/E_c$ =1.0, 1.01, and 1.05 for both Figs. 7a and 7b, and $E^* = 0.7$, 0.8, 0.9, 0.95, and 0.99 for Fig. 7c with $E_c = 1.3\times10^6$ (V/m). The dash-dash curves denote ω_{P1}^*, the dash-dot-dash curves denote ω_{P2}^*, and the solid gray curves denote ω_{P3}^*. In Fig. 7a, we have substituted the positive valued particle rotation speed, Ω, of Eq. (17) into Eqs. (24) and (25) in evaluating the spin velocity profiles. Therefore, the profiles shown in Fig. 7a are only valid within the spatial region of $0.5 < z^* \le 1$. Similarly, a negative valued Ω from Eq. (17) has been used in Eqs. (24) and (25), and thus, the spin velocity profiles shown in Fig. 7b are only valid within $0 \le z^* < 0.5$. As for Fig. 7c, the particle rotation speed is set to zero, $\Omega = 0$, in Eqs. (24) and (25). It can be seen that the spin velocity profiles evaluated at electric fields strengths of $E^* = 0.95$~1 become multi-valued in space near the middle of the flow channel (note that Ω goes to zero for $E^* = 1$ in Eq. (17)).

Figure 8. The normalized Poiseuille spin velocity profile, ω^*, plotted with respect to the spatial coordinate, z^*, evaluated at $E^* = 0$, 0.4, 0.8, 1.0, 2.0, and 3.0, with $\Gamma^* = 1$. The gray curve denotes the zero electric field value for the spin velocity, *i.e.*, the vorticity of ordinary Poiseuille flow. Note that Eqs. (45) and (47), with the proper selection of the micro-particle rotation speeds in Eq. (17), are used in the evaluation of the spin velocity for $E^* \ge 1$, whereas for $E^* \le 0.9$, Eq. (45) (with $\Omega = 0$ in Eqs. (24) and (25)) is used throughout the spatial domain of interest.

Figure 9. The normalized linear velocity profile, u^*, of Poiseuille flow with internal micro-particle electrorotation plotted with respect to the spatial coordinate, z^*, evaluated at $E^* = 0$, 0.4, 0.8, 1.0, 2.0, and 3.0, with $\Gamma^* = 1$. The gray curve denotes the zero electric field velocity

profile, which is the original Poiseuille parabolic profile. Equations (45) (*use positive* Ω *from Eq. (17) in Eqs. (24) and (25)*) and (47) (*use negative* Ω *from Eq. (17) in Eqs. (24) and (25)*) are respectively employed in the integrals of Eqs. (50a) and (50b) for $E^* \geq 1$. The evaluation of u^* for $E^* \leq 0.9$ is done by employing Eq. (45) in both Eqs. (50a) and (50b) with $\Omega = 0$ in Eqs. (24) and (25).

Figure 10. The two dimensional Poiseuille volume flow rate, Q (m^2/s), plotted with respect to the applied pressure gradient, Γ^*, evaluated at $E^* = 0$, 0.4, 0.8, 1.0, 2.0, and 3.0. The gray curve represents the zero electric field volume flow rate given by $Q_0 = \Gamma h^3/12\eta$.

Figure 11. The theoretical predictions of the volume flow rate, Q (m^2/s), versus pressure gradient, Γ (Pa/m), obtained by the present continuum treatment are compared with the experimental measurements given in Lemaire *et al.* [10] for micro-particle solid volume fractions of $\phi = 0.05$ (Fig. 11a) and 0.1 (Fig. 11b) at electric field strengths of $E_0 = 2.7$ (triangle) and 3.3 (box) (kV/mm). Using the material properties given in Ref. [10], the critical electric field for the onset of particle Quincke rotation is evaluated to be $E_c = 1.3$ (kV/mm). The diamond dotted curves represent the volume flow rates at zero electric field strengths.

Tables

Table 1.

	Electrorotation flow	Ferrofluid spin-up flow
Particles	Insulating dielectric micro-particles	Magnetic nanoparticles
Microscopic dipole	Maxwell-Wagner induced dipole	Permanent magnetic dipole
Macroscopic polarization	Retarding polarization $\overline{P}$	Magnetization $\overline{M}$
Applied field	DC electric field $\overline{E}$ (with vorticity)	Rotating magnetic field $\overline{H}$
Body torque density	$\overline{P}\times\overline{E}$	$\mu_0\overline{M}\times\overline{H}$

Table 2.

Item	Description	Value	Units
d	Micro-particle diameter	8.00×10^{-5}	m
E_c	Critical electric field strength	1.30×10^{6}	V/m
h	Channel height	1.00×10^{-3}	m
n	Particle number density	3.73×10^{11}	$1/m^3$
ε_1	Permittivity of carrier liquid	3.27×10^{-11}	C^2/Nm^2
ε_2	Permittivity of particles	2.30×10^{-11}	C^2/Nm^2
ϕ	Solid volume fraction of the particles	1.00×10^{-1}	----
η_0	Carrier liquid viscosity (no particles)	1.20×10^{-2}	$Pa\cdot s$
η'	Spin viscosity	0	$N\cdot s$
η	Zero field fluid viscosity (w/ particles)	1.53×10^{-2}	$Pa\cdot s$
η_e	$\eta_e=\eta+\zeta$	1.76×10^{-2}	$Pa\cdot s$
σ_1	Conductivity of the carrier liquid	4.00×10^{-8}	S/m
σ_2	Conductivity of the particles	1.00×10^{-14}	S/m
τ_{MW}	Maxwell-Wagner relaxation time	1.11×10^{-3}	s
ζ	Vortex viscosity	1.80×10^{-3}	$Pa\cdot s$

Tables

Table 1.

	Electrorotation flow	Ferrofluid spin-up flow
Particles	Insulating dielectric micro-particles	Magnetic nanoparticles
Microscopic dipole	Maxwell-Wagner induced dipole	Permanent magnetic dipole
Macroscopic polarization	Retarding polarization $\overline{P}$	Magnetization $\overline{M}$
Applied field	DC electric field $\overline{E}$ (with vorticity)	Rotating magnetic field $\overline{H}$
Body torque density	$\overline{P}\times\overline{E}$	$\mu_0\overline{M}\times\overline{H}$

Table 2.

Item	Description	Value	Units
d	Micro-particle diameter	8.00×10^{-5}	m
E_c	Critical electric field strength	1.30×10^{6}	V/m
h	Channel height	1.00×10^{-3}	m
n	Particle number density	3.73×10^{11}	$1/m^3$
ε_1	Permittivity of carrier liquid	3.27×10^{-11}	C^2/Nm^2
ε_2	Permittivity of particles	2.30×10^{-11}	C^2/Nm^2
ϕ	Solid volume fraction of the particles	1.00×10^{-1}	----
η_0	Carrier liquid viscosity (no particles)	1.20×10^{-2}	$Pa\cdot s$
η'	Spin viscosity	0	$N\cdot s$
η	Zero field fluid viscosity (w/ particles)	1.53×10^{-2}	$Pa\cdot s$
η_e	$\eta_e=\eta+\zeta$	1.76×10^{-2}	$Pa\cdot s$
σ_1	Conductivity of the carrier liquid	4.00×10^{-8}	S/m
σ_2	Conductivity of the particles	1.00×10^{-14}	S/m
τ_{MW}	Maxwell-Wagner relaxation time	1.11×10^{-3}	s
ζ	Vortex viscosity	1.80×10^{-3}	$Pa\cdot s$

Figure

Click here to download high resolution image

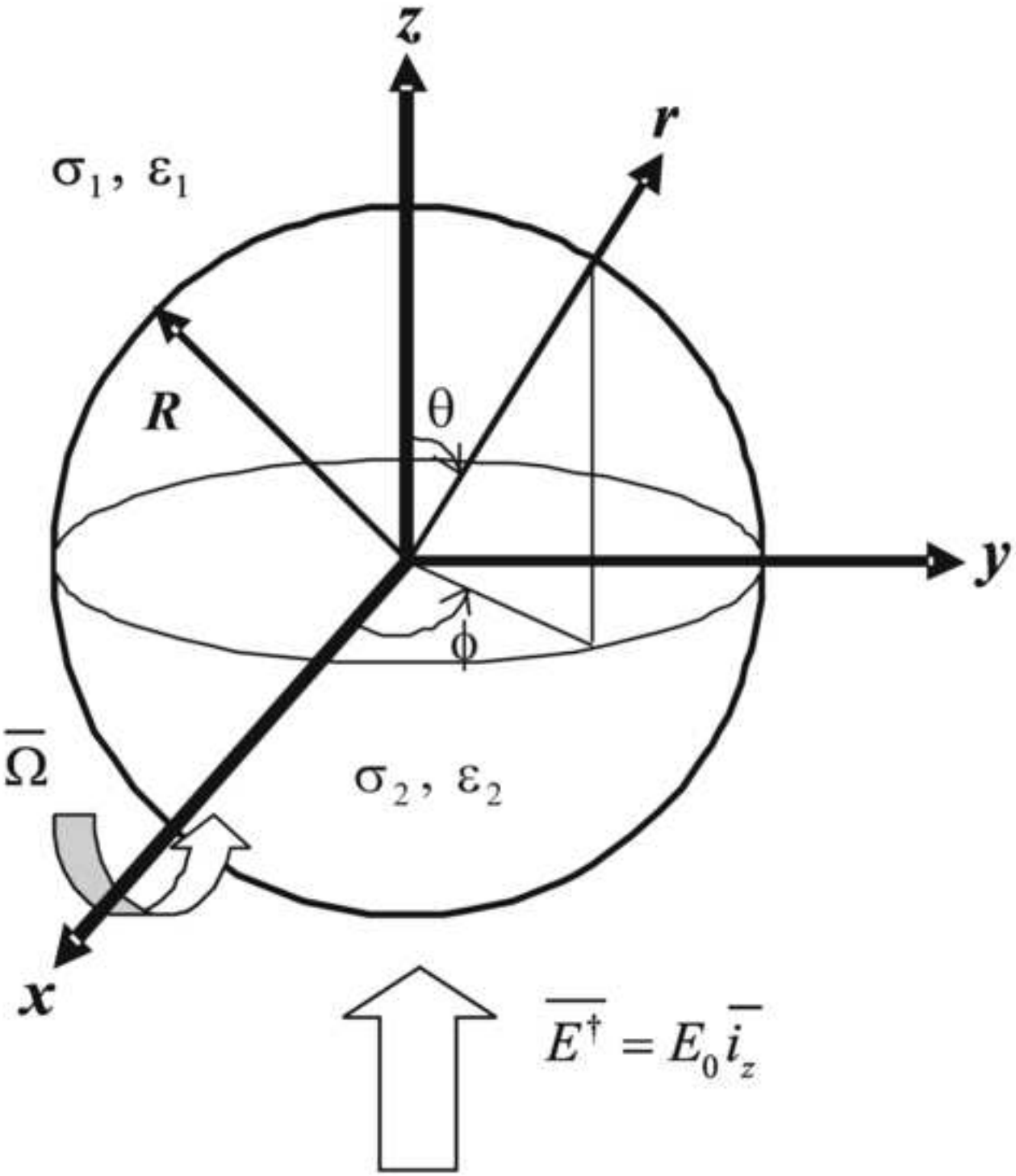

Figure

Click here to download high resolution image

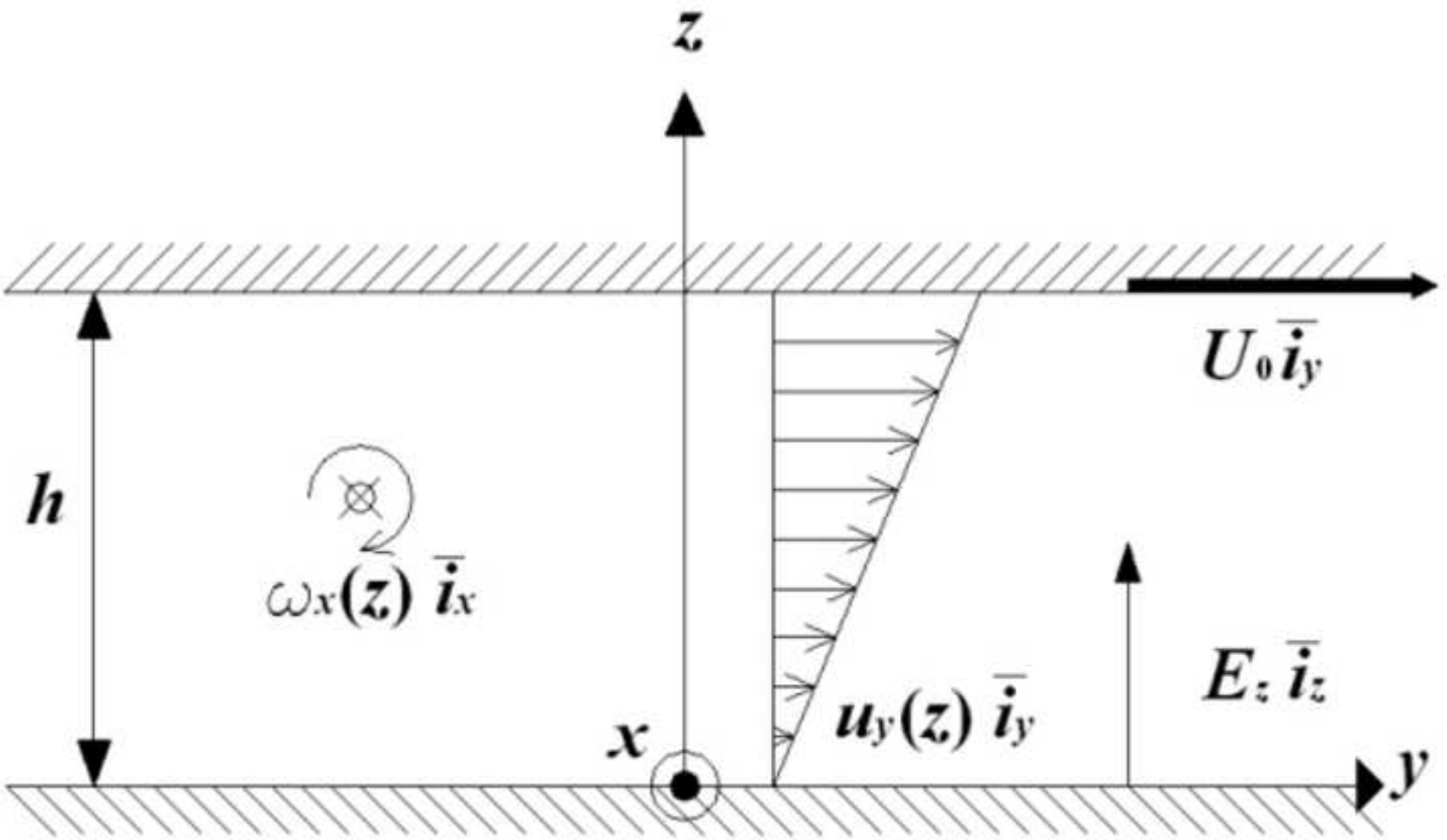

Figure
Click here to download high resolution image

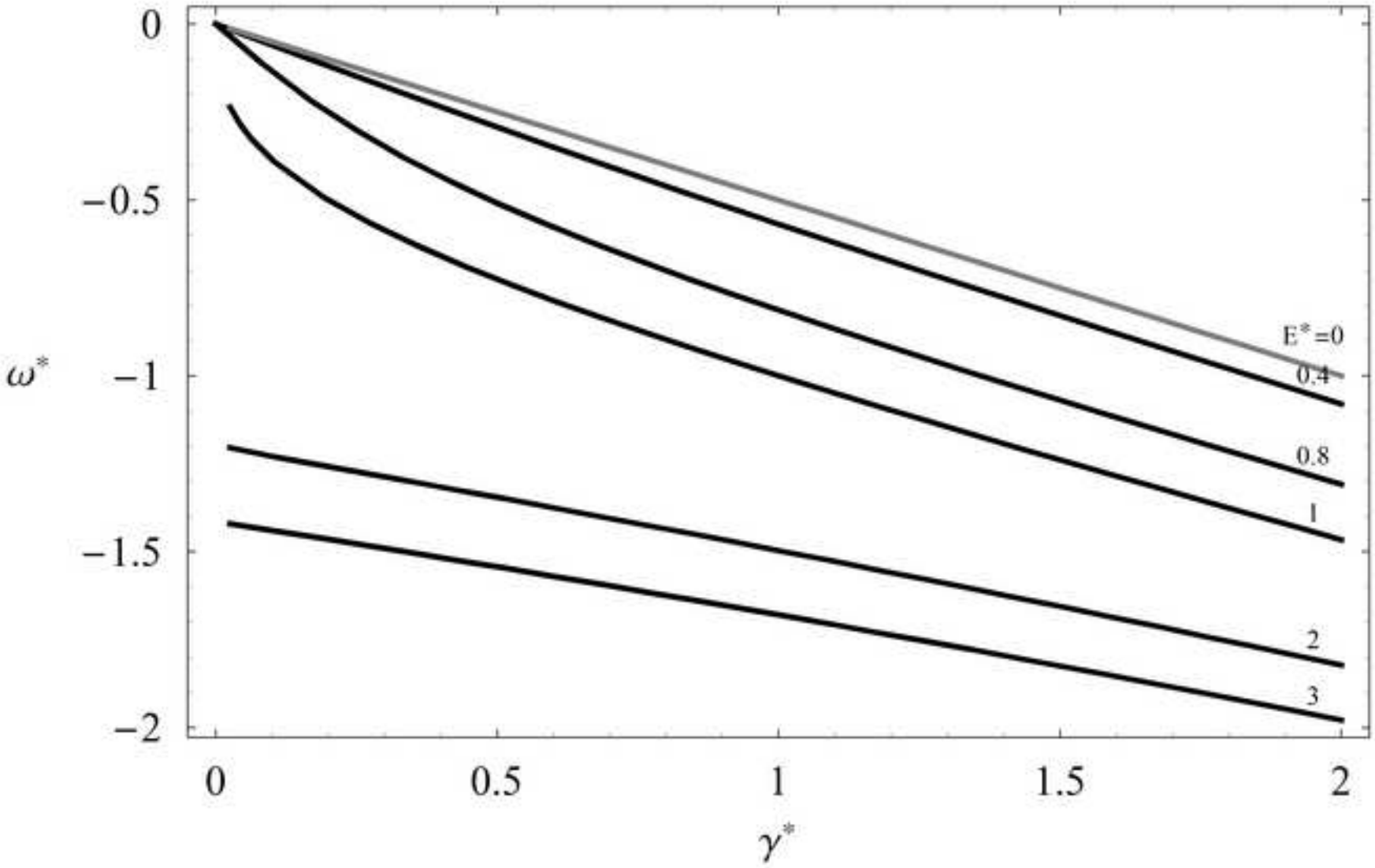

Figure
Click here to download high resolution image

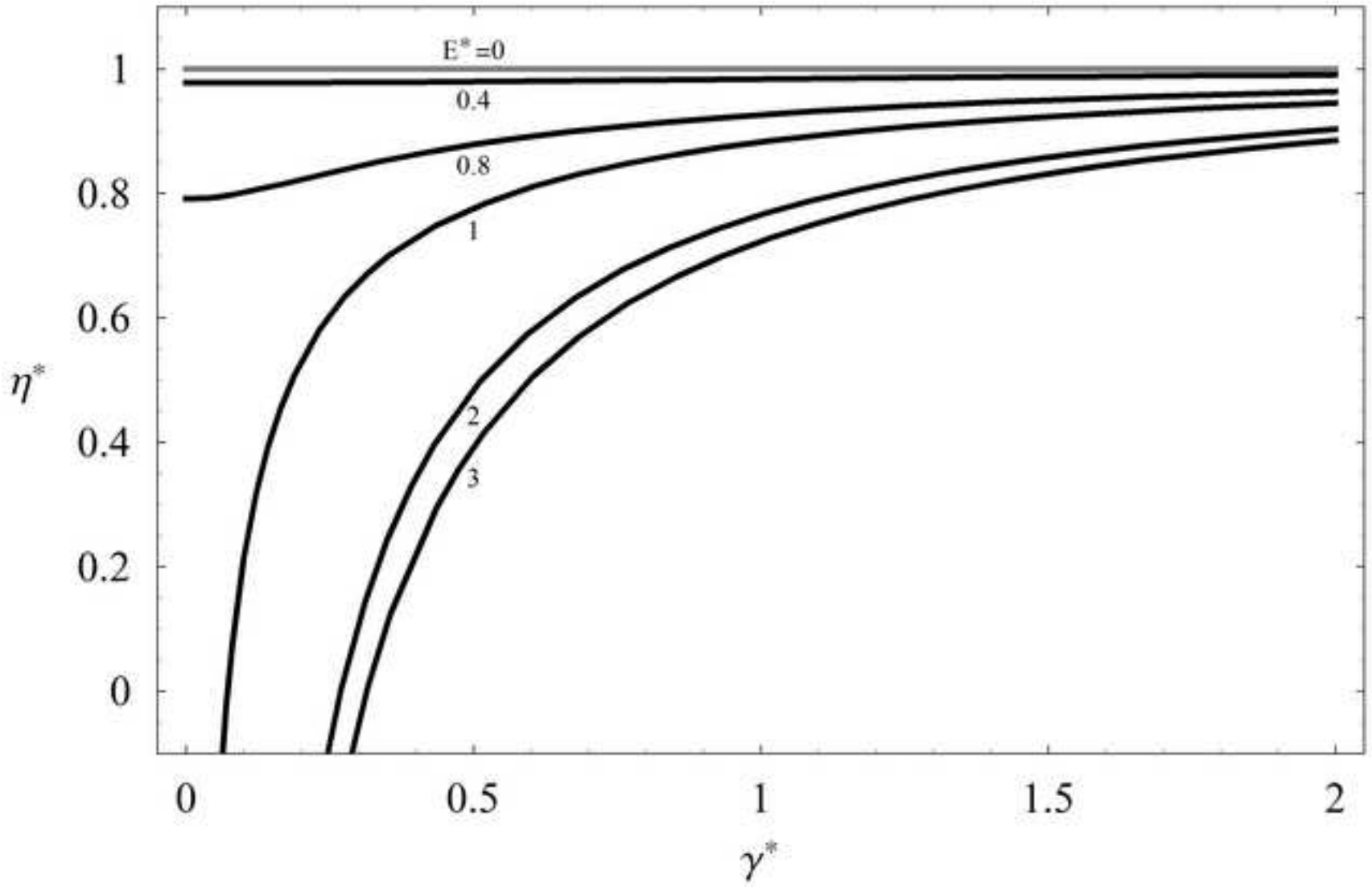

Figure
Click here to download high resolution image

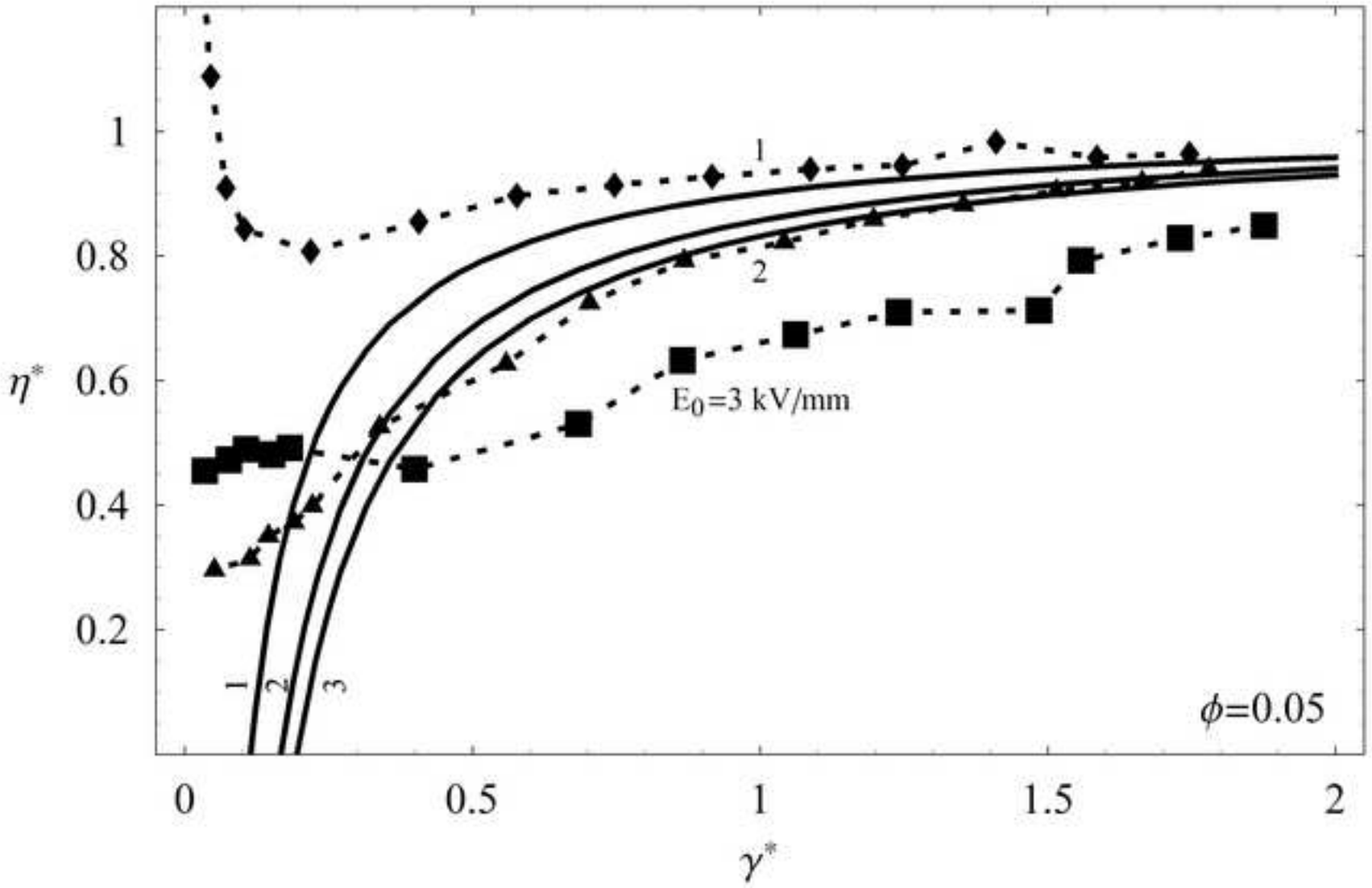

Figure
Click here to download high resolution image

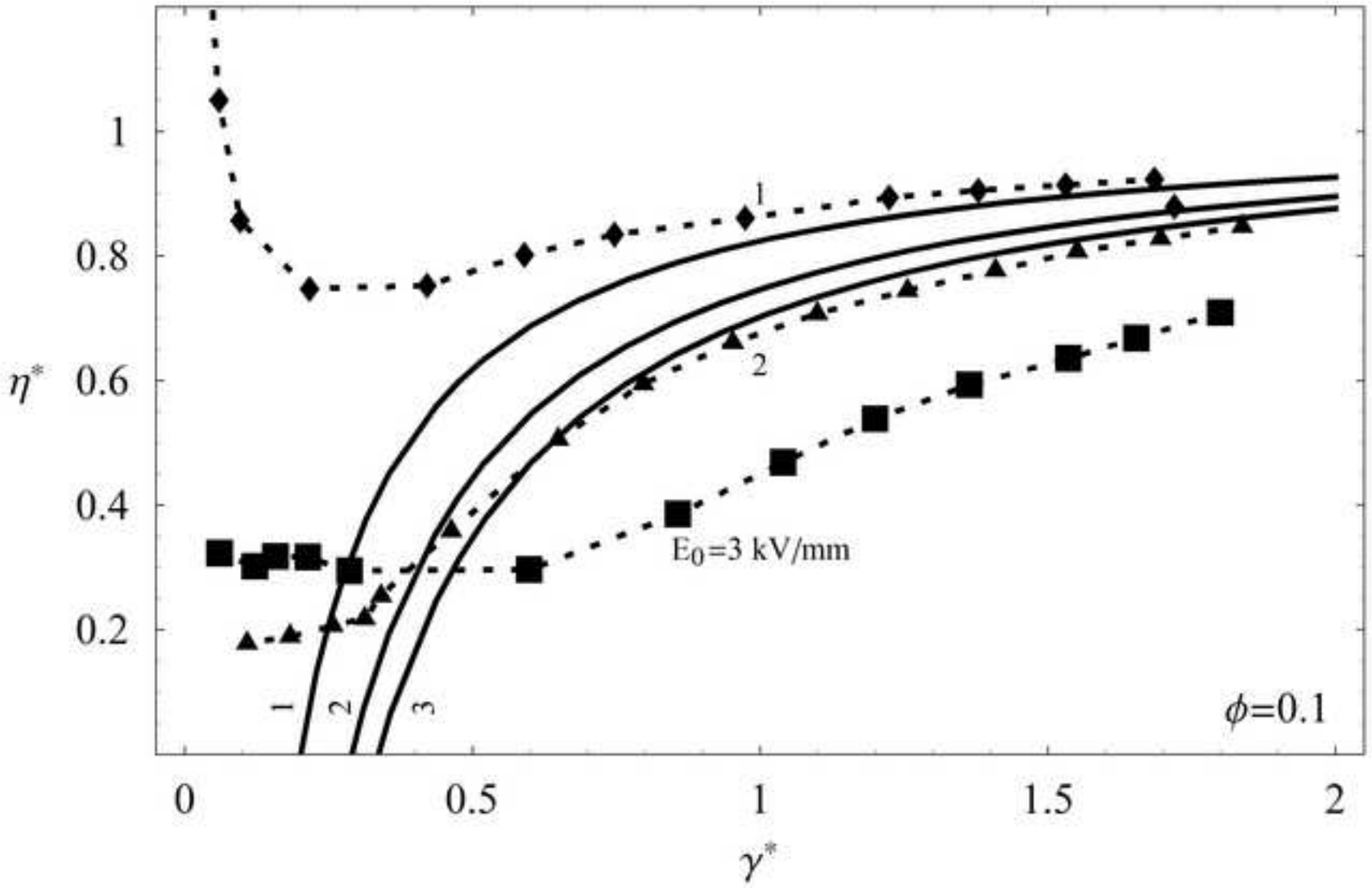

Figure

Click here to download high resolution image

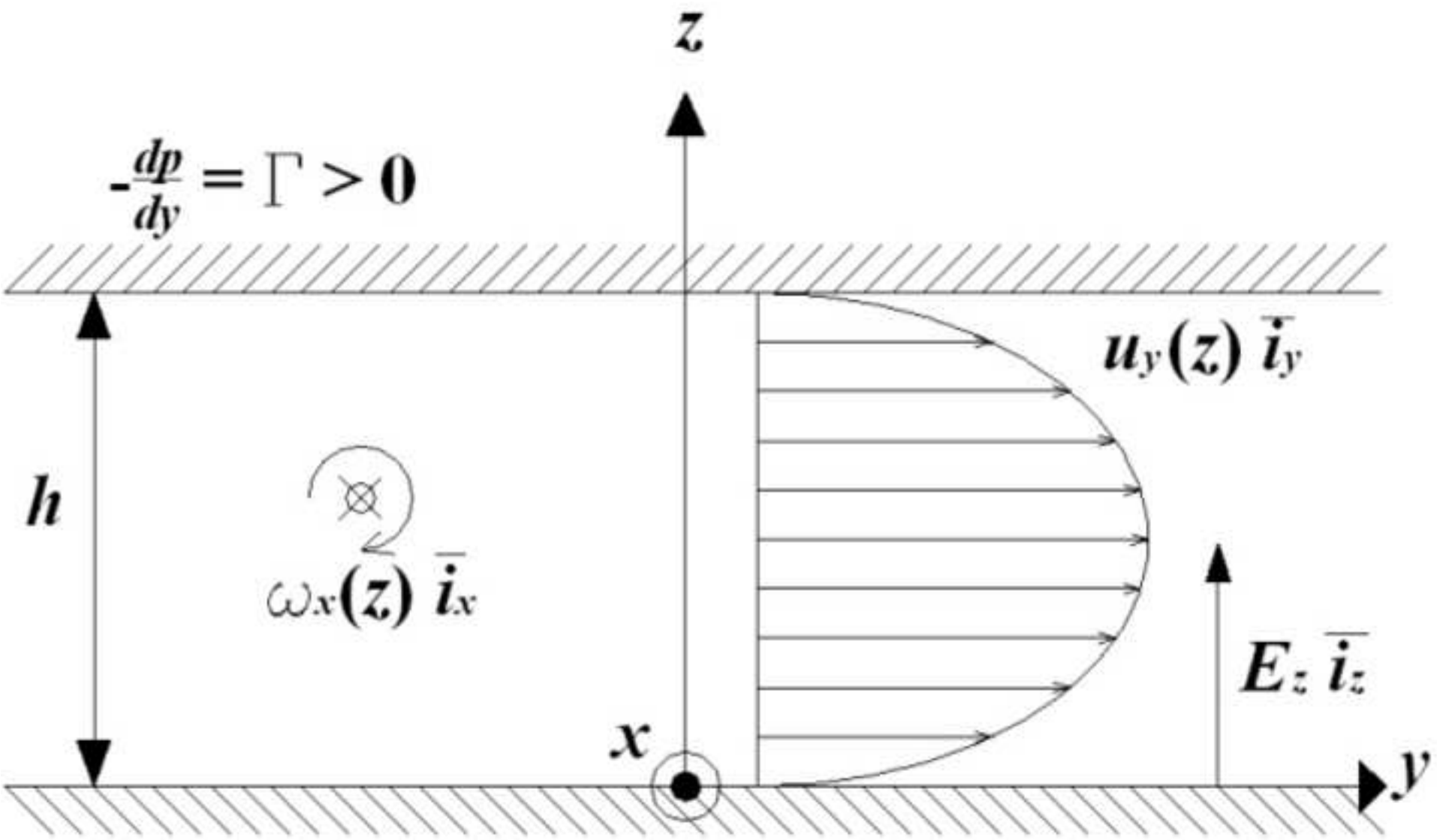

Figure
Click here to download high resolution image

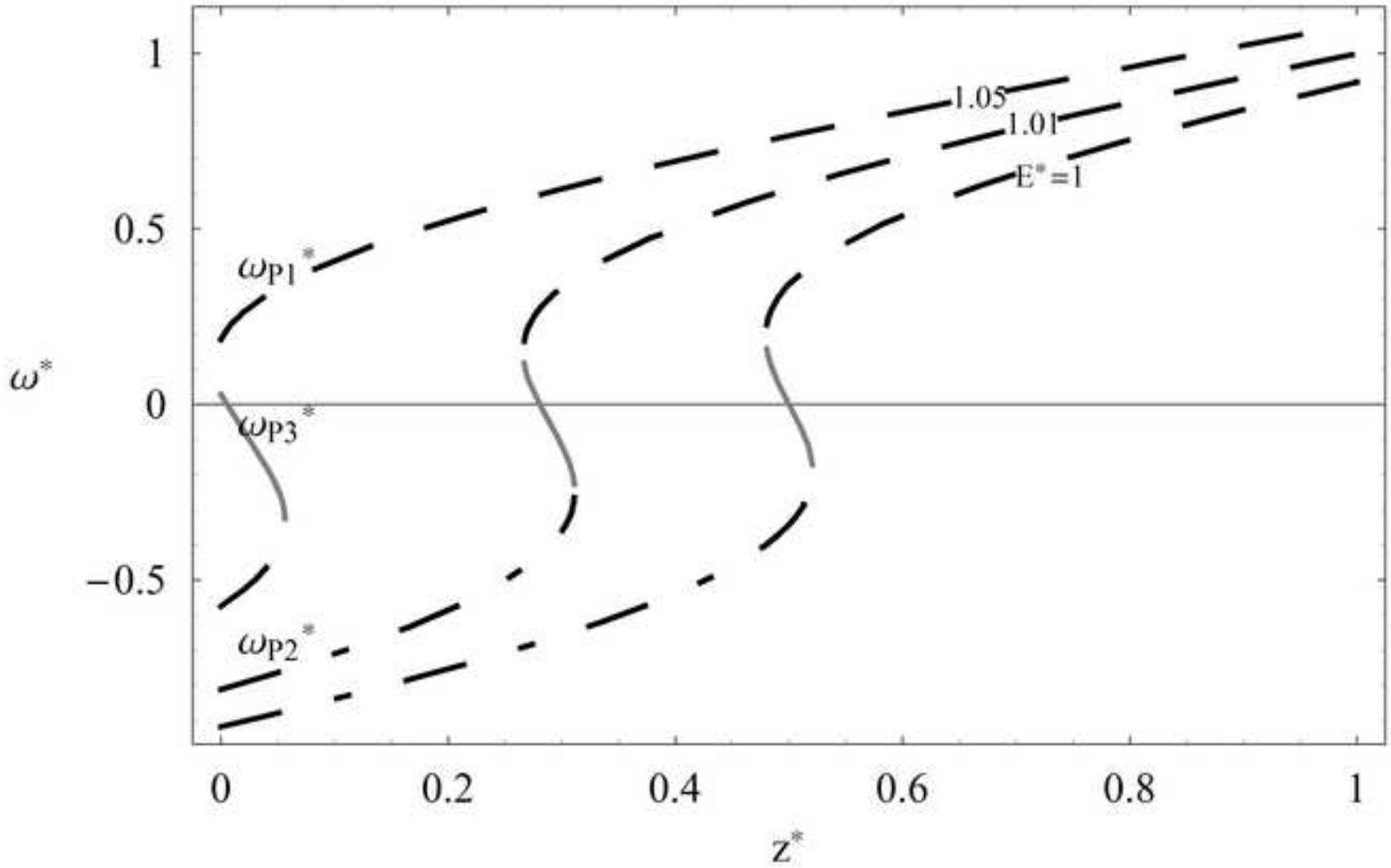

Figure

Click here to download high resolution image

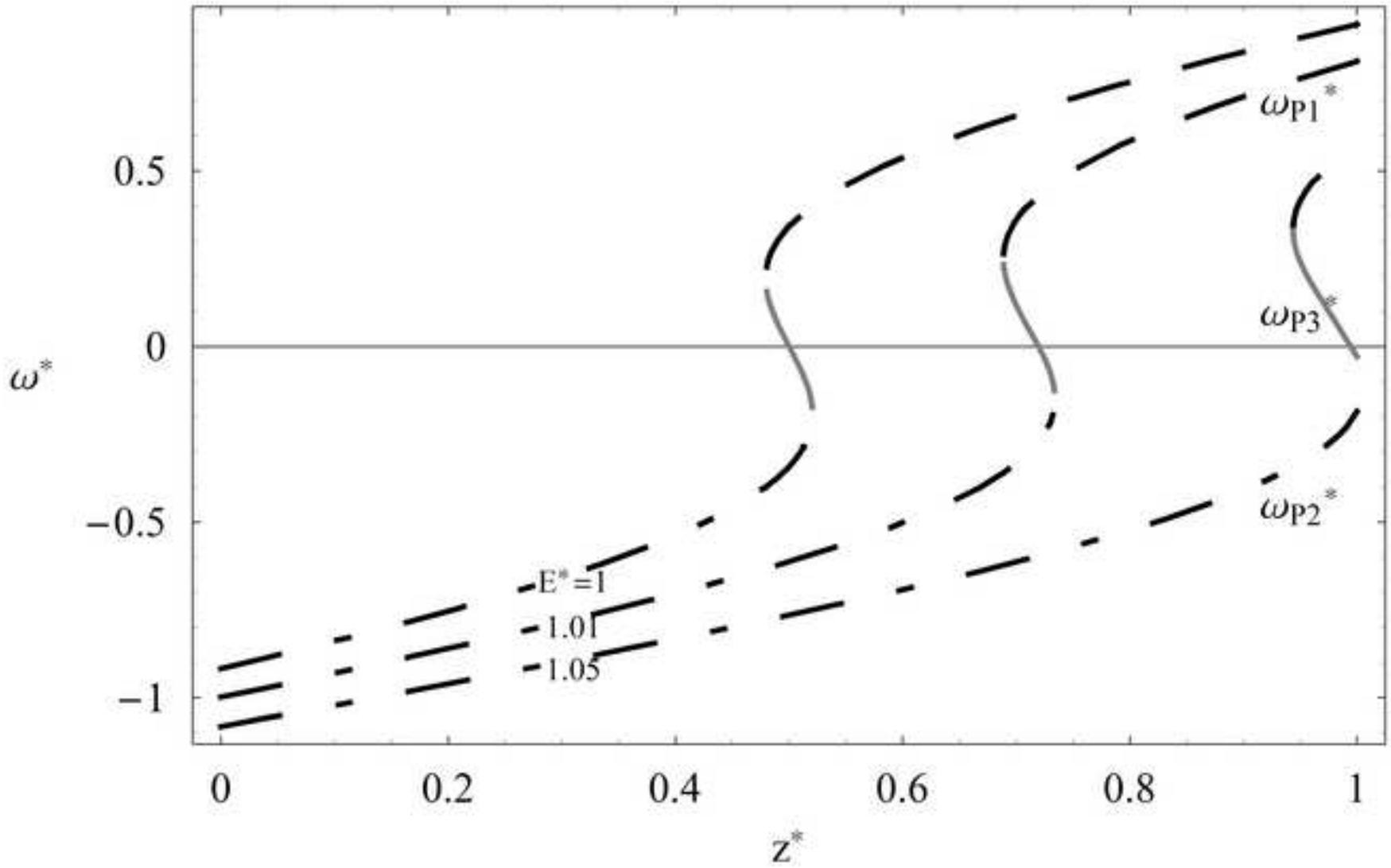

Figure

Click here to download high resolution image

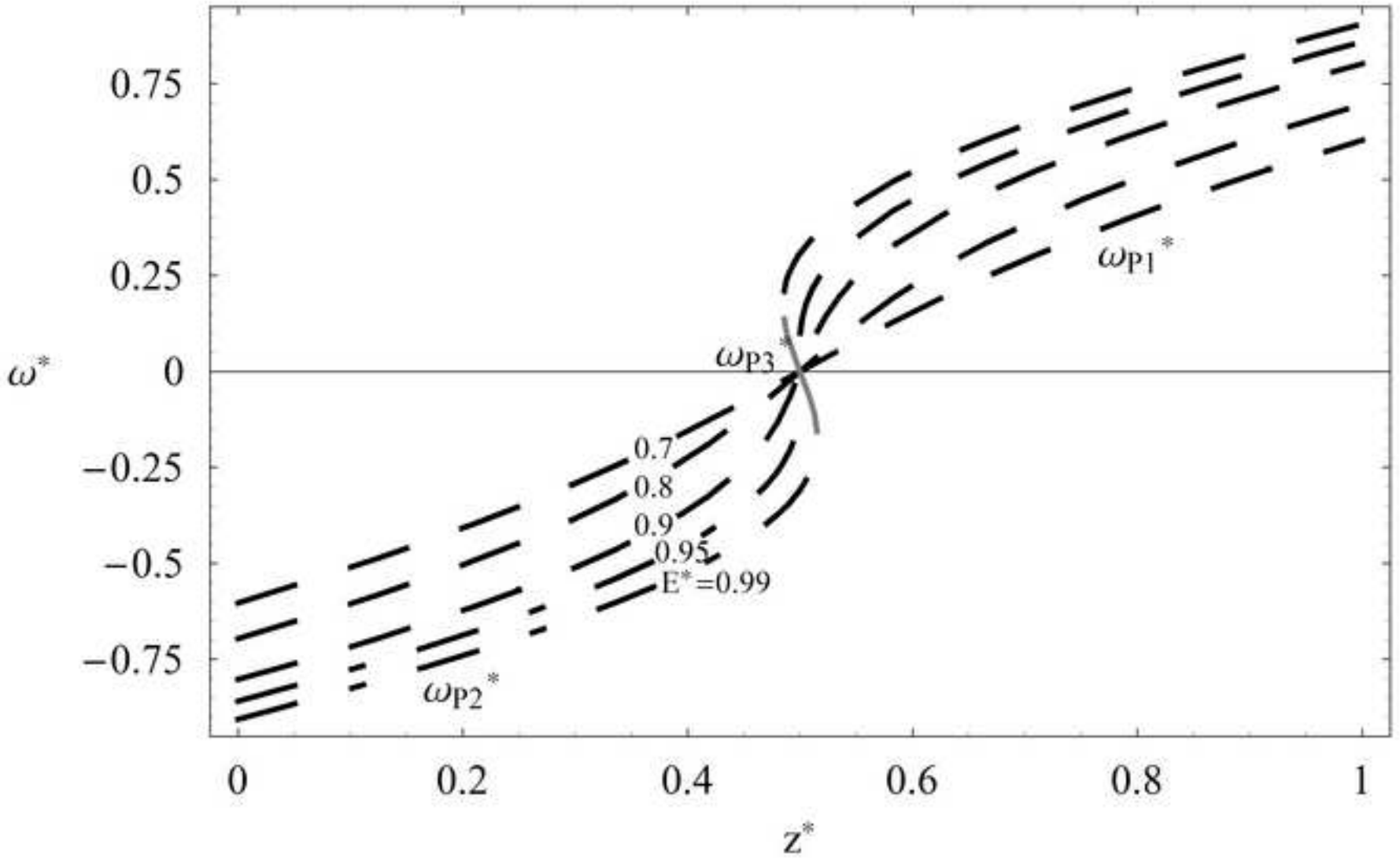

Figure
Click here to download high resolution image

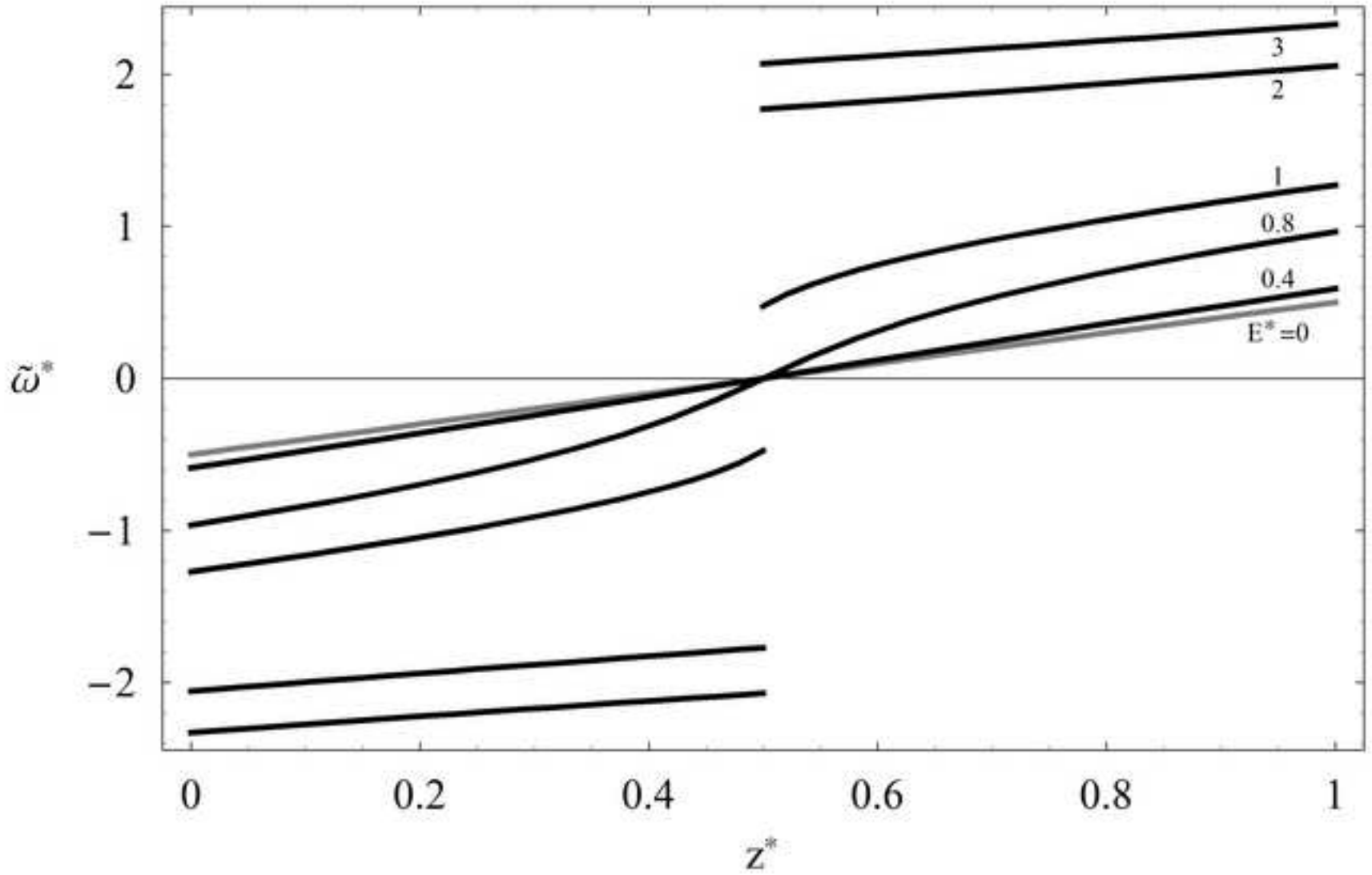

Figure
Click here to download high resolution image

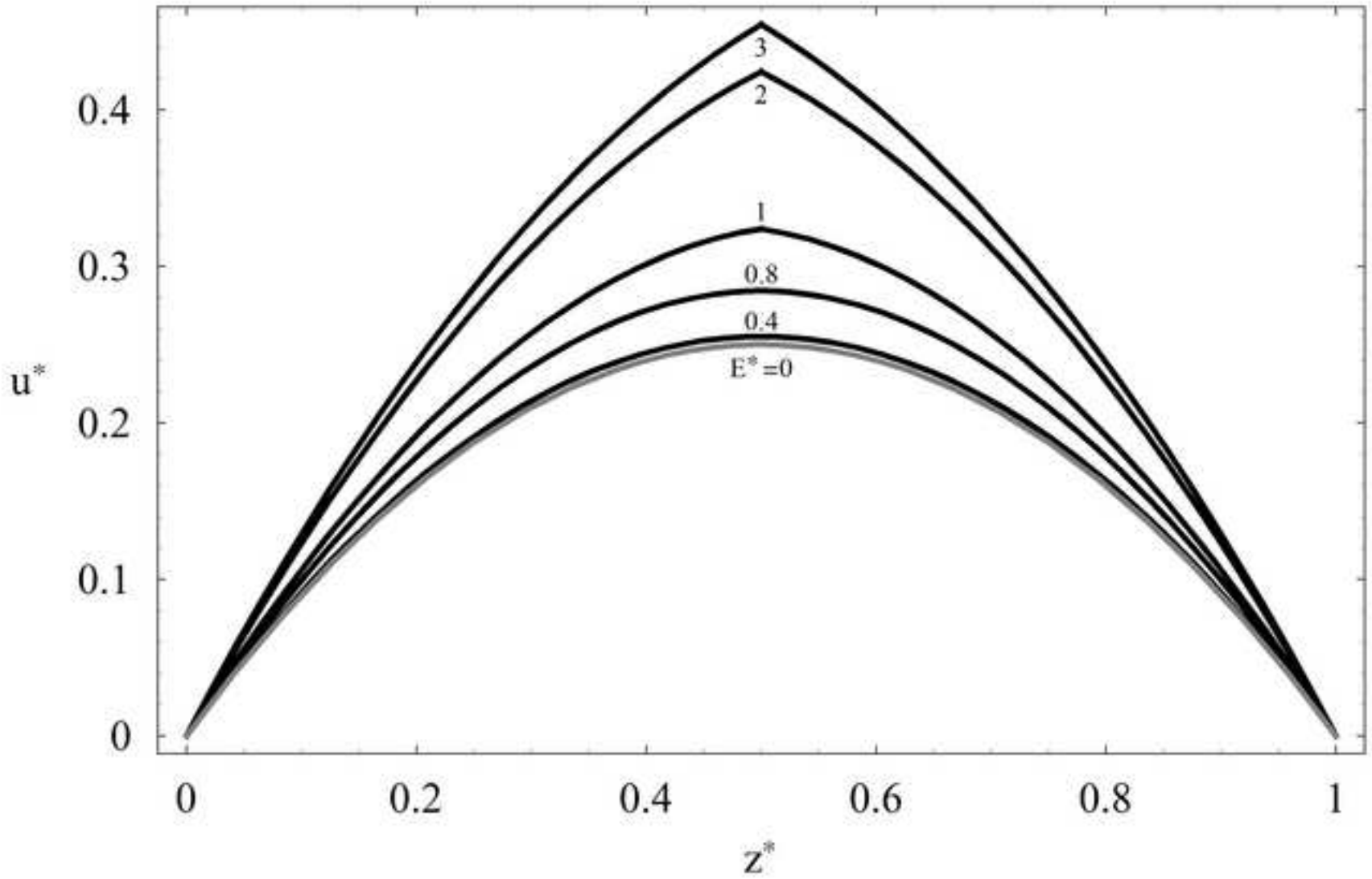

Figure

Click here to download high resolution image

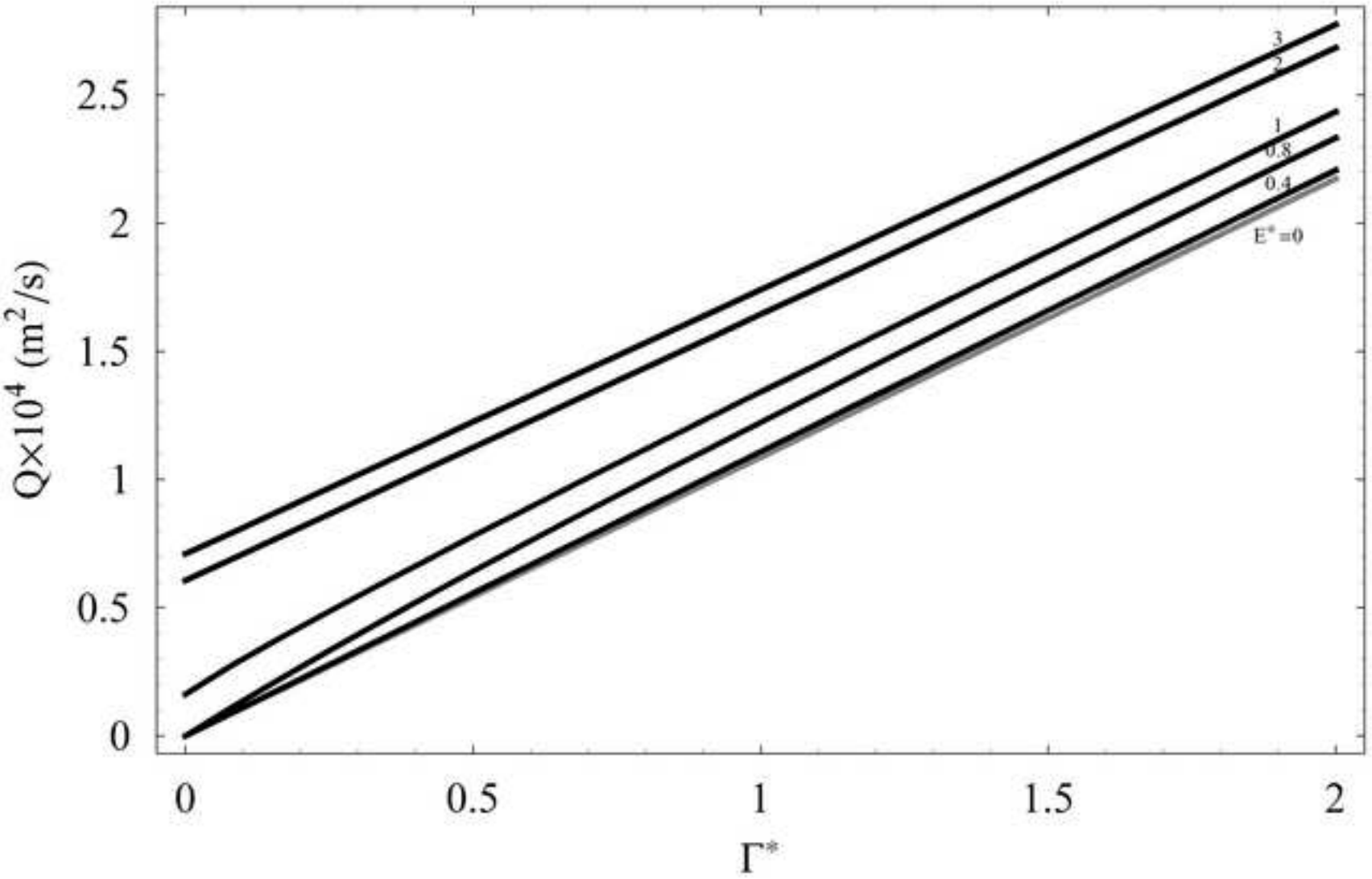

Figure

Click here to download high resolution image

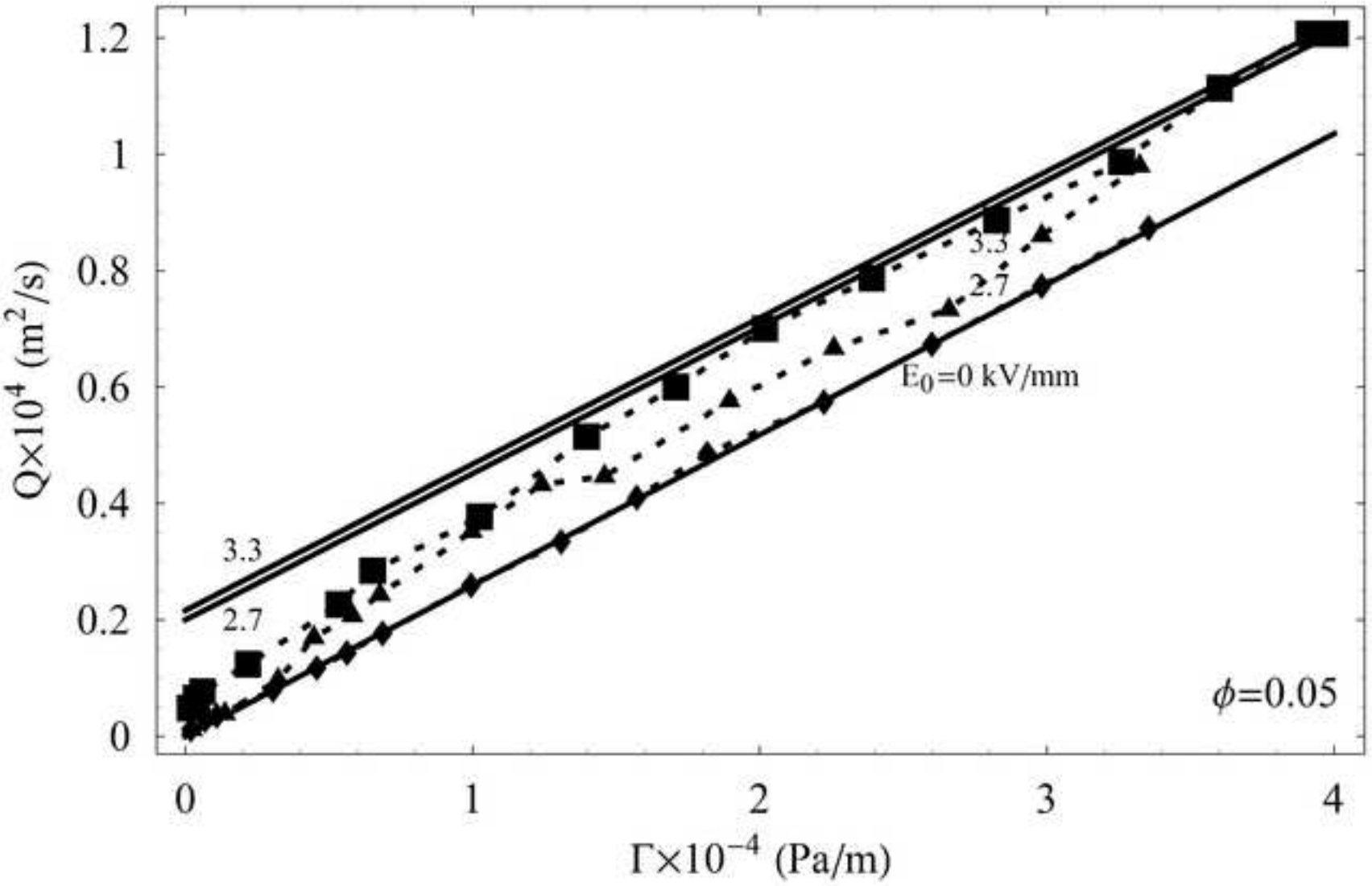

Figure

Click here to download high resolution image